MNRAS **000**, 1–18 (2016) Preprint July 18, 2022 Compiled using MNRAS LATEX style file v3.0

Evidence for a constant IMF as a function of radius in two massive ETGs

Sam P. Vaughan[1]⋆, Ryan C. W. Houghton[1], Roger L. Davies[1] and Simon Zieleniewski[1]

[1] *Astrophysics, Denys Wilkinson Building, Keble Road, Oxford, OX1 4RH*

Accepted XXX. Received YYY; in original form ZZZ

ABSTRACT

We investigate radial gradients in the stellar initial mass function (IMF) in two early type galaxies using resolved measurements of several far red gravity sensitive absorption features, including the "Wing-Ford" band (FeH). We use the Oxford Short Wavelength Integral Field SpecTrogaph (SWIFT) to obtain resolved spectroscopic observations of NGC 1277 and IC 843, two galaxies with large central velocity dispersions and evidence for "heavy" IMFs from spectroscopic and dynamical measurements. Our observations cover the IMF sensitive features sodium $\mathrm{NaI_{SDSS}}$, calcium triplet CaT as well as FeH, along with MgI 0.88 and TiO 0.89. We also use published optical indices to help untangle the degenerate parameters of age, metallicity, [α/Fe] abundance and IMF slope. Within NGC 1277 we measure a flat FeH profile at $\sim$0.38Å with a strong [Na/Fe] gradient, from which we use stellar population models to infer an old, α-enhanced population with a Chabrier IMF at all radii. IC 843 also displays a (slightly stronger) flat FeH profile at $\sim$0.4Å, which together with optical indices suggests a similarly old, α-enhanced population with a Chabrier IMF at all radii. Our results rule out bottom-heavy single power law IMFs in these objects and present galaxies which are in conflict with any simple IMF-σ relationship.

Key words: galaxies: stellar content – galaxies: elliptical and lenticular, cD

1 INTRODUCTION

The stellar Initial Mass Function (IMF) is of fundamental importance for understanding the evolution and present day stellar content of galaxies. The IMF defines the number density of stars at each mass on the zero age main sequence in a population, and is thus intricately linked to the small-scale, turbulent and not-well-understood process of star formation whilst also defining global properties for the population as a whole. The low mass end of the IMF, and hence the number of low mass stars, greatly affects the mass-to-light ratio (M/L) of a system since a large proportion of the stellar mass in a galaxy comes from stars below 1 $\mathrm{M}_{\odot}$. The fact that these low mass stars contribute so little to the integrated light of a population means that large changes in the M/L will not necessarily be reflected in large changes to the properties of the light itself. The high mass slope of the IMF makes a contribution to to a galaxy's M/L ratio too, via stellar remnants, and also defines the importance of stellar feedback and the amount of chemical enrichment that takes place. Furthermore, a form for the IMF is assumed whenever a stellar mass or star formation rate is calculated, and the implications for such observational parameters if the IMF is not universal could be very serious (e.g Clauwens et al. 2016).

Early efforts to measure the IMF were pioneered by Salpeter (1955), who used direct star counts to parametrize the IMF as a power law of the form $\xi(m) = km^{-x}$ with an exponent of $x = 2.35$. Using a single power law to describe the IMF has come to be called a "unimodal" description. The value of the Salpeter exponent at the high mass end has remained remarkably constant in the numerous studies of our own galaxy since, with modern day IMF parameterisations of the Milky Way incorporating a flattening at low masses: e.g Kroupa (2001) and Chabrier (2003). An IMF with a power law at masses greater than 0.6 $M_{\odot}$, a flat low-mass end and a spline interpolation linking the two regimes is described as a "bimodal" IMF (Vazdekis et al. 1996). The high end slope of a bimodal IMF is defined by a power law index Γ_b, which is related to x via $x = \Gamma_b + 1$.

⋆ E-mail: sam.vaughan@physics.ox.ac.uk (SPV)

Historically, little evidence was found for an IMF in our galaxy which varied depending on parameters such as metallicity or environment (see Bastian et al. (2010) for a review). More recently, however, evidence has emerged for a non-universal IMF in studies of the unresolved stellar populations of ETGs. Dynamical modelling of galaxy kinematics undertaken by Thomas et al. (2011b) as well as the ATLAS3D team (Cappellari et al. 2011) have shown that the M/L ratios of ETGs compared to the M/L ratio for a population with a Salpeter IMF diverge systematically with velocity dispersion, implying that more massive ETGs have more "bottom heavy" (dwarf enhanced) IMFs (Cappellari et al. 2013). Comparisons between stellar population synthesis models and strong gravitational lensing predict a similar IMF-σ relation (e.g. Treu et al. 2010), although massive ETGs with Milky Way-like IMFs have also been found (e.g. Smith et al. 2015a).

This work concerns a third method of studying the IMF in extragalactic objects. Certain absorption features in the spectra of integrated stellar populations vary in strength between (otherwise identical) low mass dwarf stars and low mass giants. A measurement of the strength of these "gravity sensitive" indices gives a direct handle on the dwarf-to-giant ratio and hence the low-mass IMF slope in the population. Important far red gravity sensitive absorption features include the sodium NaI doublet at 8190 Å (Faber & French 1980; Schiavon et al. 1997a), the calcium triplet (CaT: Cenarro et al. 2001) and Iron Hydride or "Wing-Ford band" at 9916 Å (FeH: Wing & Ford 1969; Schiavon et al. 1997b). Studying gravity sensitive absorption features in the spectra of ETGs in this way has a long history (e.g. Cohen 1978; Faber & French 1980; Couture & Hardy 1993; Cenarro et al. 2003), before more recent work by van Dokkum & Conroy (2010) reignited interest in the topic.

Studies of optical and far red spectral lines have suggested correlations between the IMF and [Mg/Fe] (van Dokkum & Conroy 2012, hereafter CvD12), metallicity (Martín-Navarro et al. 2015c), total dynamical density (Spiniello et al. 2015) and central velocity dispersion (La Barbera et al. 2013a), but importantly the agreement between spectral and dynamical IMF determination is unclear. Smith (2014) compared the IMF slopes derived using spectroscopic methods in CvD12 and dynamical methods in Cappellari et al. (2013) for galaxies in common between the two studies. He found overall agreement between the two methods regarding the overarching trends presented in each study, but no correlation at all between the IMF slopes determined by each group on a galaxy by galaxy basis. Additional investigation of individual galaxies using independent IMF measurements, rather than comparison of global trends between populations, is required to understand and explain this disagreement.

A more technically challenging goal in spectral IMF measurements is determining whether IMF gradients exist within a single object. Formation pathways of ETGs predict "inside-out growth", where the centre of a massive galaxy forms in a single starburst event before minor mergers with satellites accrete matter at larger radii (e.g. Naab et al. 2009; Hopkins et al. 2009, and references therein). IMF gradients can naturally arise from such a formation history if the global IMF differs between merger pairs, but few studies have presented evidence for such gradients to date. Work by La Barbera et al. measures an IMF gradient in a massive ETG with central $\sigma \sim 300\,\mathrm{kms}^{-1}$ (La Barbera et al. 2016b), whilst Martín-Navarro et al. report IMF gradients in three ETGs, including NGC 1277 studied in this work (Martín-Navarro et al. 2015a,b, hereafter MN15). Other studies make radial measurements of gravity sensitive indices but conclude in favour of individual elemental abundance gradients rather than a change in the IMF: see Zieleniewski et al. (2015), Zieleniewski et al. (2016) and McConnell et al. (2016).

In this work, we present radial observations of gravity sensitive absorption features in two galaxies. The first, NGC 1277, is a massive, compact ETG located in the Perseus cluster ($z = 0.01704$). NGC 1277 is a well studied object. It has been named as a candidate "relic galaxy" due to its similarity with ETGs at much higher redshifts (Trujillo et al. 2014), seen controversy over the mass of its central black hole (e.g. see van den Bosch et al. 2012 compared to Emsellem 2013) and had radial measurements of its IMF gradient taken, found using optical and far red absorption indices (MN15). Their study didn't extend to measurements of the FeH index, however. MN15 found a bottom heavy bimodal IMF at all radii, measuring the slope of the IMF to be $\Gamma_b \sim 3$ (the same high-mass slope as a unimodal power law with $x = 4$) in the central regions and dropping to $\Gamma_b \sim 2.5$ ($x = 3.5$) at radii greater than 0.6 R_e.

The second galaxy, IC 843, is an edge on ETG located on the edge of the Coma cluster ($z = 0.02457$). Thomas et al. (2007) conducted a study of the dark matter content of 17 ETGs in Coma, finding that IC 843 had an unusually high mass-to-light ratio in the R_c band with the best fitting model implying that mass follows light in this system. This result could be explained by a bottom heavy IMF, but also by a dark matter distribution where the dark matter closely follows the visible matter. Spectral measurements of the IMF slope in IC 843 will be able to break this degeneracy. Both galaxies were chosen because the evidence for their heavy IMFs implies that the Wing-Ford band could be particularly strong in these objects.

We follow Conroy & van Dokkum (2012) in our naming convention of IMF slopes: a Chabrier IMF corresponding to that in the Milky Way disc (defined in Chabrier 2003), a "bottom light" IMF defined in van Dokkum (2008), a Salpeter power law IMF with $x = 2.35$ (from Salpeter 1955) and a "bottom heavy" IMF with $x = 3$. Notice that the Chabrier and bottom-light IMFs in the CvD12 models are not simple power laws, but have a turn over and flattening at low masses very similar to a bimodal IMF. When deriving IMF slope values in this paper, we call a single power law with x=1.8 a "Chabrier-like" IMF, following Spiniello et al. (2014).

This paper is organised as follows. Section 2 summarises our observations and section 3 describes the data reduction process, including details of sky subtraction and telluric correction. We summarise our radial index measurements in section 4, present analysis and discussion in sections 5 and 6 and draw our conclusions in section 7. Appendices contain further discussion of our telluric correction and sky subtraction techniques. We adopt a ΛCDM cosmology, with H_0=68 kms^{-1}, Ω_m=0.3 and Ω_Λ=0.7.

Table 1. Targets and Observations

Galaxy	D (Mpc)	Ra	Dec	z	R_e (kpc)	Obs. Date	Integration Time (s)
NGC 1277	74.4	03:19:51.5	+41:34:24.3	0.01704	1.2	27th Jan 2016	7 × 900
IC 843	107.9	13:01:33.6	+29:07:49.7	0.02457	4.7	17th Mar 2016	9 × 900

Table 2. Definitions of the feature bandpass and blue and red pseudo-continuum bandpasses for each index studied in this work, from Cenarro et al. (2001) and CvD12. The NaI_{SDSS}definition is from La Barbera et al. (2013a). Since it is a ratio between the blue and red pseudo-continuua, the TiO index has no feature bandpass definition. All wavelengths are measured in air.

Index	Blue Continuum (Å)	Feature (Å)	Red Continuum (Å)
NaI_{SDSS}	8145.2-8155.2	8182.3-8202.3	8235.3-8246.3
CaT	8474.0-8484.0	8484.0-8513.0	8563.0-8577.0
	8474.0-8484.0	8522.0-8562.0	8563.0-8577.0
	8619.0-8642.0	8642.0-8682.0	8700.0-8725.0
MgI	8777.4-8789.4	8801.9-8816.9	8847.4-8857.4
TiO	8835.0-8855.0	—	8870.0-8890.0
FeH	9855.0-9880.0	9905.0-9935.0	9940.0-9970.0

2 OBSERVATIONS

We used the Short Wavelength Integral Field specTrograph (Thatte et al. 2006, SWIFT) on January 27th 2016 and March 17th 2016 to obtain deep integral field observations of NGC 1277 and IC 843. Observations were taken in the 235 mas spaxel^{-1} settings, giving a field-of-view of 10.3″ by 20.9″. The wavelength coverages extends from 6300 Å to 10412 Å, with an average spectral resolution of R∼4000 and a sampling of 1 Å pix^{-1}. Dedicated sky frames, offset by ∼100″ in declination, were observed in an OSO pattern to be used as first order sky subtraction. The seeing ranged between ∼1″ and 1.5″ throughout. Table 1 lists details of the targets and observations.

The wavelength range of SWIFT allows for measurements of the NaI_{SDSS}, CaII triplet, MgI and FeH (Wing Ford band) absorption features, as well as MgI 0.88 and TiO 0.89. Definitions of pseudo-continuum and absorption bands for each index are given in Table 2, taken from Cenarro et al. (2001) and van Dokkum & Conroy (2012). We use the definition of NaI_{SDSS} from La Barbera et al. (2013a).

3 DATA REDUCTION

The data were reduced using the SWIFT data reduction pipeline to perform standard bias subtraction, flat-field and illumination correction, wavelength calibration and error propagation. Cosmic ray hits were detected and removed using the LaCosmic routine (van Dokkum 2001).

Differential atmospheric refraction causes the centre of the galaxy to change position within a datacube as a function of wavelength. Although the magnitude of this effect is small (leading to a ∼1″ shift at red wavelengths for the observations which are lowest in the sky), individual cubes were corrected by interpolating each wavelength slice to a common position. The individual observation cubes were combined using a dedicated python script, which linearly interpolates sub-pixel offsets between the frames.

3.1 Telluric Correction and Sky Subtraction

At the redshift of these galaxies, telluric absorption is prevalent around the MgI and TiO features in both objects and near the blue continuum band of the NaI_{SDSS} feature in NGC 1277. We used the ESO tool MOLECFIT (Kausch et al. 2014) to remove it from our spectra. MOLECFIT creates a synthetic telluric absorption spectrum based on a science observation contaminated by telluric absorption. Using the radiative transfer code of Clough et al. (2005), a model line-spread function of the instrument used to observe the data and a model atmospheric profile based on the temperature and chemical composition at the time and place of observation, a telluric spectrum is fit to the science spectra and then divided out. We use MOLECFIT between the regions λλ 7561-7768 Å, 81212-8338Å and 8931-9875 Å.

Variations in night sky emission lines occur on similar timescales to our observations, meaning that significant residuals from telluric emission remain after first order sky subtraction. This is especially true in the far red end of the spectrum. These residuals are the main source of systematic uncertainty in the measurement of the FeH band, and so must be accurately subtracted to ensure robust index measurements at 1μm. We use two independent sky subtraction methods in this work: removing skylines whilst simultaneously fitting kinematics, and fitting each wavelength slice of our observation cubes with a model galaxy profile and sky image before subtracting the best fit sky model.

3.1.1 Removing Skylines with `pPXF`

The first sky subtraction technique uses the method of penalised pixel fitting (Cappellari & Emsellem 2004, `pPXF`) to fit sky spectra to our data at the same time as fitting the stellar kinematics, as discussed in Weijmans et al. (2009) and Zieleniewski et al. (2016). This involves passing `pPXF` a selection of sky templates (as well as stellar templates) which are scaled to find the best fit linear combination to the remaining sky residuals.

The sky templates were extracted from the dedicated sky frames observed throughout the night. To account for flexure, each sky template was shifted forward and backwards in wavelength by up to 2.5 pixels (2.5 Å). Note that the `pPXF` sky subtraction occurs *after* first order sky-subtraction, and so we also include negatively-scaled sky spectra in the list of templates in order to fit negative residu-

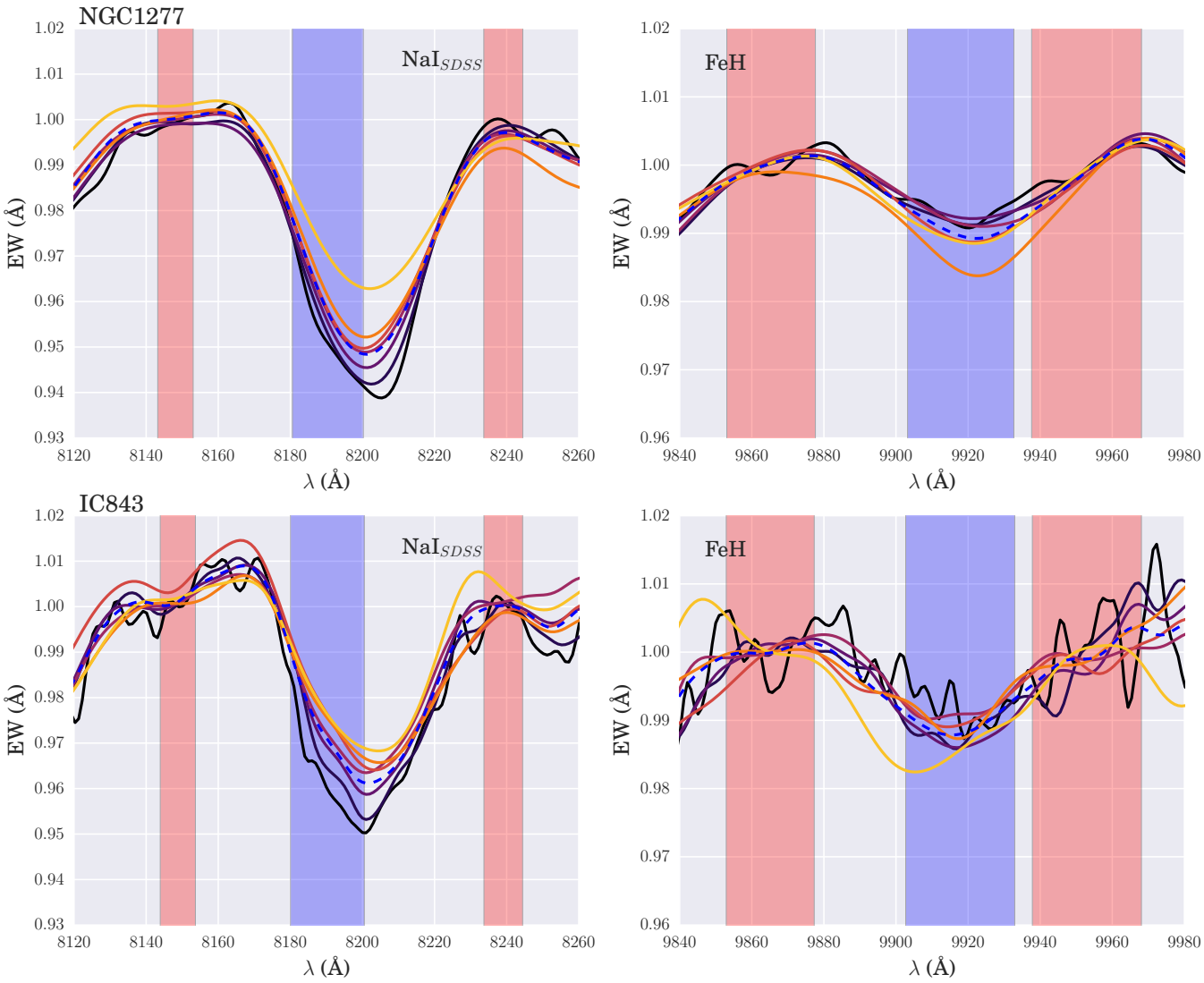

Figure 1. Plots of the spectra around the dwarf sensitive indices NaI8190 and Wing-Ford band (FeH) for NGC 1277 (top) and IC 843 (bottom). Spectra are coloured from dark (central bin) to light (outskirts) and are convolved up to a common velocity dispersion of 450 kms^{-1} (NGC 1277) and 300 kms^{-1} (IC 843) for display purposes only. The dotted blue line is the global spectrum for each galaxy. Blue and red shaded regions show the index band and continuum definitions respectively.

als (which correspond to over-subtracted skylines). The sky spectra were also split into separate regions around emission lines caused by different molecular transitions, based on definitions from Davies (2007). We also introduced a small number of further splits to the sky spectrum by eye, around areas where skyline residuals changed sign. Each region was allowed to vary individually in `pPXF` to achieve the best sky subtraction.

The choice of sky splits makes a noticeable difference to the quality of sky subtraction, especially around the feature most contaminated by sky emission, the Wing-Ford band. Correspondingly, the sky split selection has a non-negligible effect on the FeH index measurement. We selected the total number and location of cuts to the sky spectrum around FeH by quantifying the residuals of the sky subtracted spectrum around the best-fitting `pPXF` template for various sky split combinations. We chose the combination of sky splits which had a distribution containing fewest catastrophic outliers (i.e most similar to a Normal distribution), both by eye and quantified using the Anderson-Darling test statistic (Anderson & Darling 1954). This process is discussed in further detail in Appendix A.

3.1.2 *Median Profile Fitting*

The second sky subtraction method is independent of the first. Each observation cube (which has undergone first order sky subtraction) is a combination of galaxy light and residual sky light. In each wavelength slice, sky emission corresponds to an addition of flux in all pixels whereas galaxy light is concentrated around the centre of the observation. We aim to model these two contributions in a single data cube and subtract off the best fitting sky model.

We take the median image of the data cube as the galaxy model in our fitting procedure. This assumes that the shape of galaxy light profile doesn't change over the

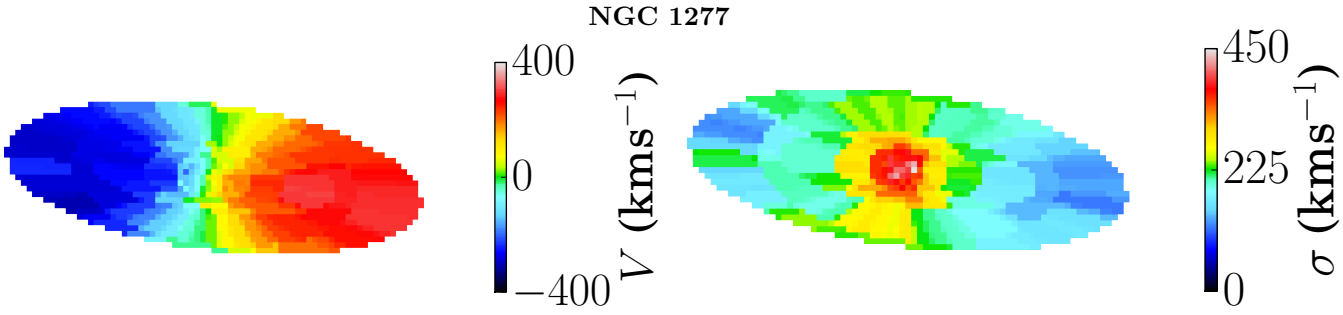

(a) Velocity. The peak velocity is ± 320 kms^{-1}.

(b) Velocity Dispersion. The central σ is 420 kms^{-1}.

Figure 2. NGC 1277 Kinematic Maps. The data were binned using the Sector Binning algorithm of Vaughan et al. 17 (in prep) to a S/N ratio of 15 per bin. The CvD template library around the CaII triplet was used in `pPXF` to measure V and σ.

SWIFT wavelength range of 6300 Å to 10412 Å, but is only scaled up and down as the galaxy gets brighter or dimmer and the instrument throughput varies. The sky model is a flat image, constant at each pixel.

Using a simple least squares algorithm, we fit the galaxy and sky model to each wavelength slice of an individual O-S cube simultaneously. We then subtract the best fit sky residuals for each cube, combine the cubes as before and are left with an alternative sky subtracted data cube for each galaxy. These are binned and passed to `pPXF` to measure the kinematics as before, except without using the sky subtraction technique of Section 3.1.1.

The median profile fitting method leads to slightly noisier results than using `pPXF`, and as such all index measurements quoted in this paper are derived from the first sky subtraction method. However our conclusions are unchanged regardless of which sky subtraction technique we employ. A comparison of the two methods is presented in Appendix A.

3.2 Index Measurements

To attain a signal to noise (SN) ratio high enough to robustly measure equivalent widths, we binned the data cubes into elliptical annuli of uniform SN, which were then split in half along the axis of the galaxy's rotation. The kinematics in each bin were measured using `pPXF`, after which each half of the same annulus was interpolated back to its rest frame and added together. This leads to a roughly constant SN in each bin for each index. Spectra of the 3 IMF sensitive indices studied in this work, for each radial bin in both galaxies, are shown in Figure 1.

The equivalent widths of absorption features depend on the velocity dispersion of the spectrum they are measured from. A larger velocity dispersion tends to "wash out" a strong feature, leading to a smaller equivalent width. In order to compare measurements between different radii in the same galaxy, as well as between separate galaxies, we correct each index measurement to a common σ of 200 kms^{-1} using the same method as Zieleniewski et al. (2016).

Equivalent widths are measured using the formalism of Cenarro et al. (2001), which measures indices relative to a first order error-weighted least squares fit to the pseudo-continuum in each continuum band. We propagate errors from the variance frames of each observation by making a variance spectrum for each science spectrum, and error bars show 1σ uncertainties.

4 RESULTS

4.1 Kinematics

We used `pPXF` and the stellar template library of CvD12 to measure the kinematics of NGC 1277 and IC 843. The Sector Binning technique of Vaughan et al. (2017, in prep) is used to bin the observations into elliptical annuli and divide each annulus into angular sectors, reaching a SN of at least 15 in the galaxy outskirts. The three CaII absorption features at 8498, 8542 and 8662 Å are measured to determine the rotation velocity and velocity dispersion in each bin. The kinematic maps are shown in Figures 2 and 3. Future work will use these kinematic measurements to to calculate Jeans models and dynamical M/L ratios, in order to make a dynamical measurement of the IMF in NGC 1277 and IC 843.

Both galaxies are fast rotators, with peak rotation velocities reaching ± 300 kms^{-1} in NGC 1277 and ± 200 kms^{-1} in IC 843. The central velocity dispersion in NGC 1277 is remarkably high at ∼420 kms^{-1}, in agreement with the values measured by MN15. Kinematic results derived by placing a pseudo-slit across the 2D kinematic maps are shown in Figure 4, along with the long-slit results from MN15.

4.2 Index Equivalent Widths

Figure 5 shows the results of measuring the IMF sensitive absorption features in NGC 1277 and IC 843 as a function of radius. As discussed in Section 3.2, these measurements were taken at the intrinsic velocity dispersion of the radial bin and then corrected to 200 kms^{-1} for both galaxies. All results are equivalent widths, in units of Å and found using the formalism of Cenarro et al. (2001), except for that of TiO which is a ratio of the blue and red pseudo-continuua.

4.2.1 NGC 1277

NGC 1277 shows an unusually strong Na absorption feature at 8190 Å in its centre, which drops from ∼ 1.2 Å to ∼ 0.75Å at 6.5″ (∼1.9 R$_e$, 2.27 kpc). This behaviour is consistent with the findings of MN15, who found a similarly

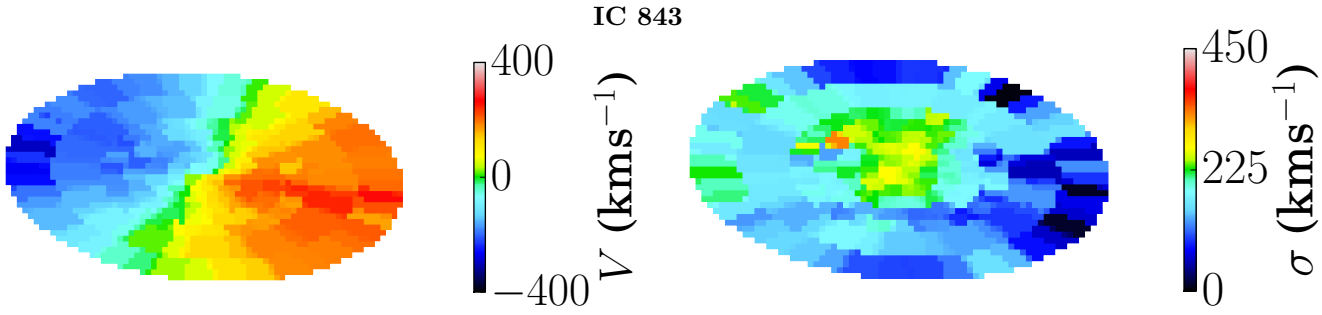

(a) Velocity. The peak velocity is ± 220 kms^{-1}.

(b) Velocity Dispersion. The central σ is 260 kms^{-1}.

Figure 3. IC 843 Kinematic Maps. Same as Figure 2 , except binned to a SNR of 20.

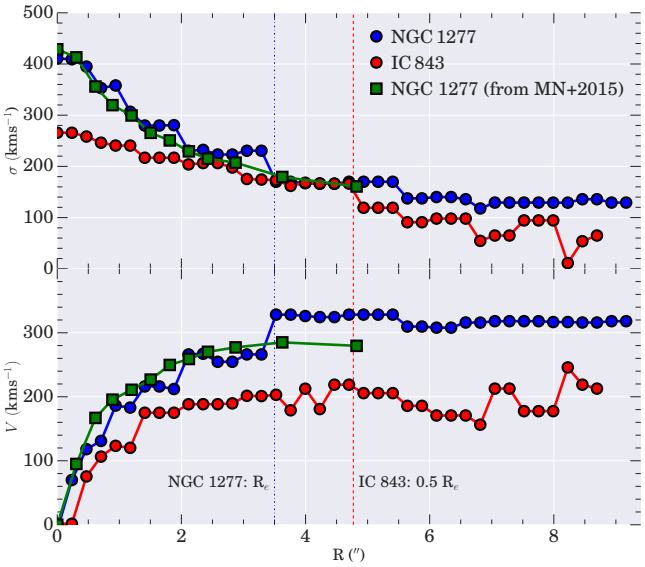

Figure 4. Kinematic parameters for IC 843 (red) and NGC 1277 (blue), derived by placing a pseudo-slit along the kinematic maps shown in Figures 2 and 3. Both galaxies show large central velocity dispersions (especially NGC 1277, with σ=410 kms^{-1}) and ordered rotation at larger radii. Green points are long-slit observations of NGC 1277 taken from MN15.

strong Sodium absorption gradient in this galaxy. The CaT shows almost no radial departure from the central value of 7.0 Å for the central 3″ before decreasing to 6.25 Å in the outskirts.

No gradient in FeH is evident; the points scatter around 0.4 Å at all radii. We measure a decrease in TiO from 1.08 Å to 1.06 Å, with the MgI results scattering around 0.5 Å at all radii.

4.2.2 IC 843

A strong gradient in Na exists in IC 843, dropping from a central value of 0.8 Å to 0.5 Å at ∼3″ (∼0.31 R$_e$, 1.49 kpc). A very slight negative gradient in CaT is seen, from 7.4 Å to 6.9 Å at 5.5″.

FeH also shows no obvious gradient, with a similar value of 0.4 Å as that measured in NGC 1277. We measure a gradient in TiO, dropping from 1.07 Å in the centre to 1.06 Å at 1 R$_e$, and our MgI measurements are flat at 0.55 Å for all radii.

5 ANALYSIS

5.1 Prior Results from Optical Indices

We use the models of Thomas et al. (2011a) and previously published optical index measurements of NGC 1277 and IC 843 to constrain the age, [α/Fe] and [Z/H] of both galaxies. The models give Lick absorption line indices for a range of metallicities, ages and [α/Fe] abundances whilst assuming a Salpeter IMF. Varying abundances of C, N, Mg, Na, Si, Ca, Ti, Cr and Fe are also modelled, based on the index response functions of Korn et al. (2005). Specifically, we plot <Fe>-Mgb and [MgFe]′-H$_\beta$ maps, where <Fe> is the average of the Lick Fe52 and Fe53 indices whilst [MgFe]′ is defined by Thomas et al. (2005).

IC 843 has integrated optical index measurements from its central 3″ published by Price et al. (2011). We use the resolved measurements of Ferré-Mateu (2016, in prep.) for radial optical index values in NGC 1277. The [MgFe]′-H$_\beta$ and <Fe>-Mgb maps for these data are shown in Figures 6a and 6b respectively, where all data points and models are at the Lick resolution.

In Figure 6a, we plot [MgFe]′ against H$_\beta$ with a model grid from Thomas et al. (2011a) overlaid. Shown are solar α-abundance populations, increasing in age from 3 Gyrs (dark, top) to 15 Gyrs (light, bottom). Metallicity increases from left (sub solar) to right ([Z/H] =+0.67 dex) along the lines. IC 843 is measured to have [Z/H] of greater than solar (∼0.2 dex) and an old population, consistent with an age of 10 Gyr. NGC 1277 shows surprisingly low H$_\beta$ measurements, especially in its centre, which correspond to very old stars. We measure a gradient in [Z/H], from +0.35 in the centre falling to slightly super solar at 2.35 R$_e$.

Figure 6b shows <Fe>-Mgb, with lines representing a fixed age of 13 Gyrs, metallicity increasing along the lines and [α/Fe] varying from sub-solar (dark blue, top) to super solar (orange, bottom). We find that IC 843 is consistent with [Z/H]=+0.2, in agreement with Figure 6a, and [α/Fe]∼+0.3. NGC 1277 again displays a metallicity gradient, from [Z/H]∼0.4 in the centre dropping to slightly above solar at 1.35 R$_e$, and is consistent with [α/Fe]∼=+0.3 at all radii.

We therefore adopt fiducial population parameters of 13.5 Gyr age, metallicity of [Z/H]=+0.2 and [α/Fe]∼+0.3 for IC 843 whilst NGC 1277 shows an age of 13.5 Gyr and [α/Fe]∼+0.3 at all radii, with a gradient in [Z/H] from +0.4 to +0.1 at 1.35 R$_e$. Our adopted NGC 1277 parameters are

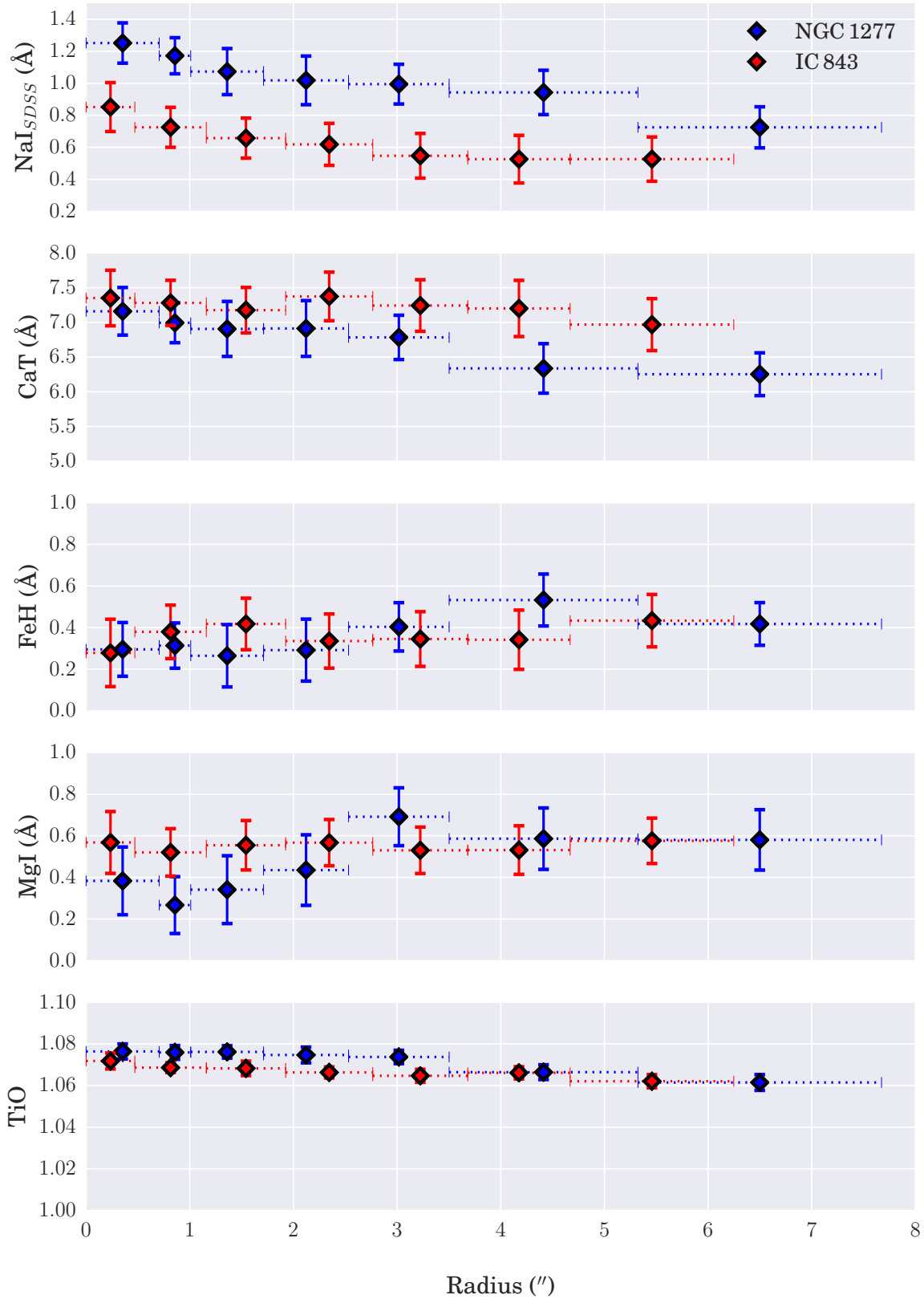

Figure 5. Radial measurements for each index in NGC 1277 (blue) and IC 843 (red). All equivalent width measurements have been corrected to a common velocity dispersion of 200 kms^{-1} (see section 3.2).

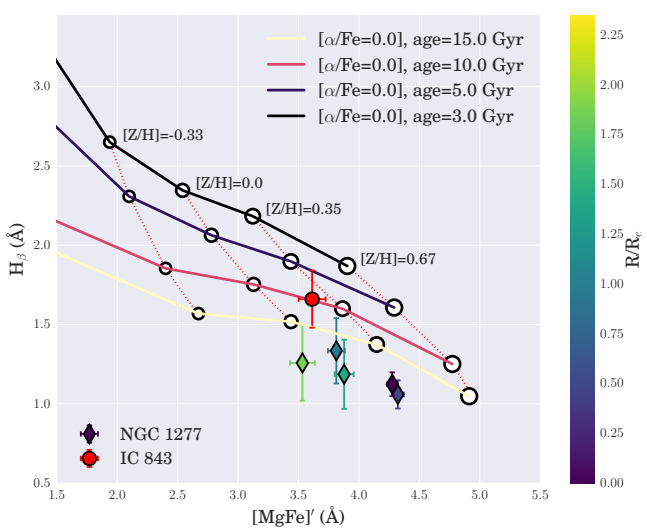

(a) H_β-[MgFe]′ index map showing radial measurements for NGC 1277 from Ferré-Mateu (2016, in prep.) as diamonds coloured according to their radial position. An integrated measurement of the central 3″ of IC 843 from Price et al. (2011) is shown as a red circle. Lines are solar α-abundance population models from Thomas et al. (2011a) at various ages. Metallicity increases from left to right along the lines, whilst age increases from 3 Gyrs (dark, top) to 15 Gyrs (light, bottom). Both galaxies are found have old populations, and we assume an age of 13.5 Gyrs for both at all radii. Note that the low Hβ strength in NGC 1277 might be caused by weak emission.

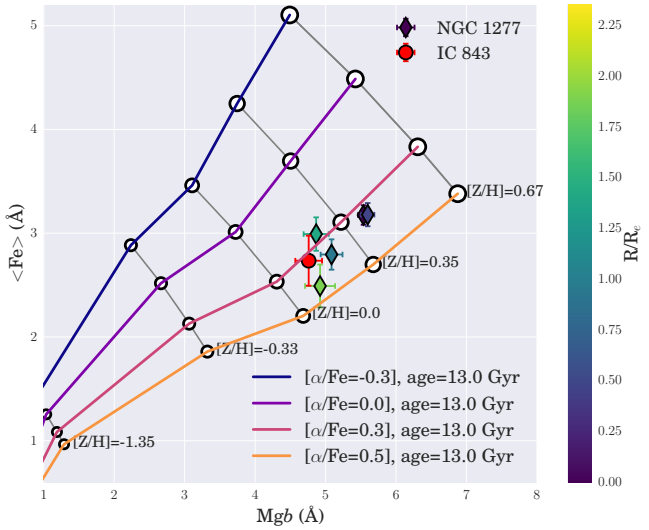

(b) As for Figure 6a, but showing MgB against <Fe>. Lines are 13 Gyr population models from the SPS models of Thomas et al. (2011a) at various [α/Fe] abundance values. Metallicity increases from left to right along the lines, whilst [α/Fe] increases from dark blue (top) to orange (bottom). IC 843 is shown to have an [α/Fe] enhancement of +0.3 at [Z/H]=∼+0.3. NGC 1277 has [α/Fe]=+0.3 at all radii and a metallicity gradient from +0.4 in the centre to slightly above solar at $2.35R_e$.

in agreement with the values found from the full spectral fitting approach of MN15 (their Figure 4).

5.2 Far red indices

We now compare our far red index measurements to the SPS models from CvD12 in order to measure the IMF in these objects. The models are single stellar population template spectra from 1500-24000 Å at a resolution of R∼2000, covering changes in IMF slope from "bottom-light" to "bottom heavy" ($x = 3$), varying age from 3 to 13.5 Gyr and enhancements in [α/Fe] from solar to +0.3 dex. Additionally, 17 elemental abundance ratios [X/Fe] can be increased or decreased by a factor of 2 from from a 13.5 Gyr, Chabrier IMF and solar [α/Fe] population. Whilst this "base" SSP is at solar metallicity, SSPs with variations in [α/Fe], age and [X/Fe] are calculated at fixed [Fe/H]=0.0 rather than fixed [Z/H]=0.0. This means that the total metallicity [Z/H] changes according to the relation from Trager et al. (2000):

$$[\mathrm{Fe/H}] = [\mathrm{Z/H}] - 0.93 \times [\alpha/\mathrm{Fe}] \quad (1)$$

Equation 1 implies that the CvD12 models are not fully representative of populations with varying metallicity, since only α elements are increased. We try to account for this fact when deriving IMF slopes for each galaxy in section 6.2.

Figures 6 and 7 show index-index plots of TiO-FeH (top) and MgI-NaI$_{\mathrm{SDSS}}$ (bottom) for NGC 1277 and IC 843, with model predictions from van Dokkum & Conroy (2012) showing variations in IMF slope, age, [α/Fe] enhancement and individual element abundances. Both models and data are corrected to a common velocity dispersion of 200 kms^{-1}. Data points are coloured according to their radial position, from dark (centre) to light (outskirts).

5.3 NGC 1277

The top panel of Figure 6 shows the TiO-FeH Index-Index plot for NGC 1277. The points scatter around an [α/Fe] enhanced Chabrier IMF for this system, with the global spectrum strongly rejecting a bottom heavy unimodal IMF due to the measured strength of the Wing Ford band. A slight radial trend towards smaller alpha enhancement is evident, which could also be explained by a small abundance gradient in [Ti/Fe]. Whilst the TiO feature strength could be explained by a 3 Gyr old population with solar alpha abundance, this is ruled out by the optical index measurements.

The bottom panel shows the MgI-NaI$_{\mathrm{SDSS}}$ map for this galaxy. Due to residual telluric contamination, our MgI measurements are quite uncertain but are fairly consistent with an [α/Fe] enhancement in agreement with with the TiO-FeH map. The NaI$_{\mathrm{SDSS}}$ measurements point to either a large enhancement in [Na/Fe] in the centre, an IMF slope much steeper than $x = 3$ at all radii, or a combination of the two. Following the strength of the FeH band, we propose the former explanation: a strong [Na/Fe] enhancement and a Chabrier IMF slope (see Section **??**). The alternative interpretation of a very bottom heavy unimodal IMF would require a huge under-abundance of [Fe/H] ($\gg$ 0.3 dex) to match the FeH measurements. Since there is no evidence for this based on the optical, iron sensitive indices Fe52 or Fe53, we rule out this scenario.

We can find the maximum amount of [Na/Fe] enhancement consistent with the data by assuming a Chabrier IMF slope at all radii. Since our NaI$_{\mathrm{SDSS}}$ measurements lie out-

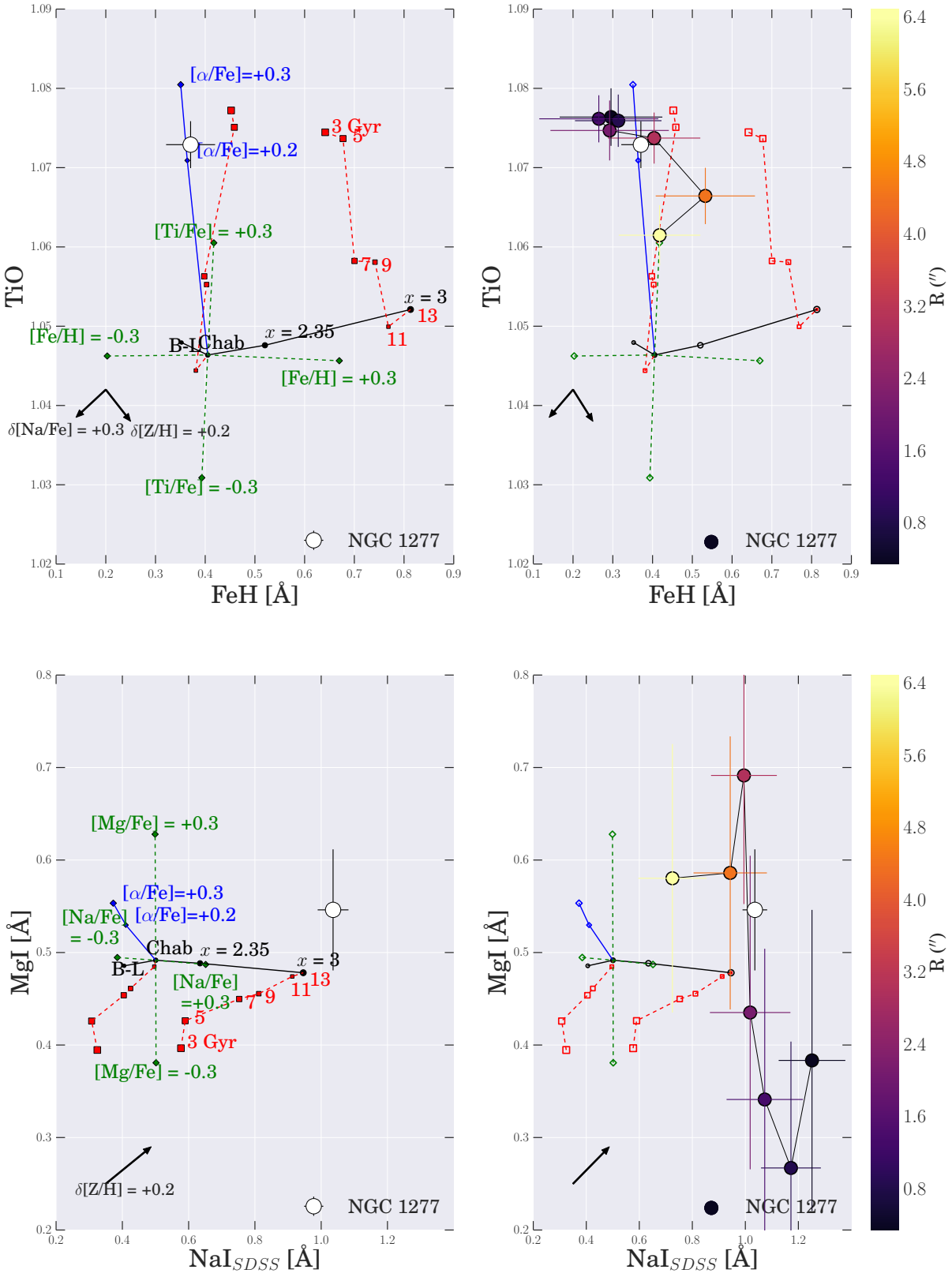

Figure 6. Index-Index maps of TiO-FeH (top) and MgI-NaI$_{\rm SDSS}$(bottom), showing radial variation in line strengths for NGC 1277. The left hand column shows the position of the global measurement for each map whilst the right hand column shows radial variations. Radial measurements are coloured from dark (centre) to light (outskirts) and all points are corrected to a common velocity dispersion of 200 kms^{-1}. Lines show variation in age, alpha enhancement, individual element abundances and IMF slope, based on the SSP models of van Dokkum & Conroy (2012). The black arrows show the index responses to changes in total metallicity and sodium abundance for a Chabrier IMF. These are derived from the SPS models of Vazdekis et al. (2015) (the FeH response is approximated from the vector shown in Fig. 10 of La Barbera et al. 2016b) and the CvD12 models respectively. For NGC 1277 we infer a Chabrier IMF with a strong [Na/Fe] enhancement in an [α/Fe] enhanced population (see Section 5.3 for details).

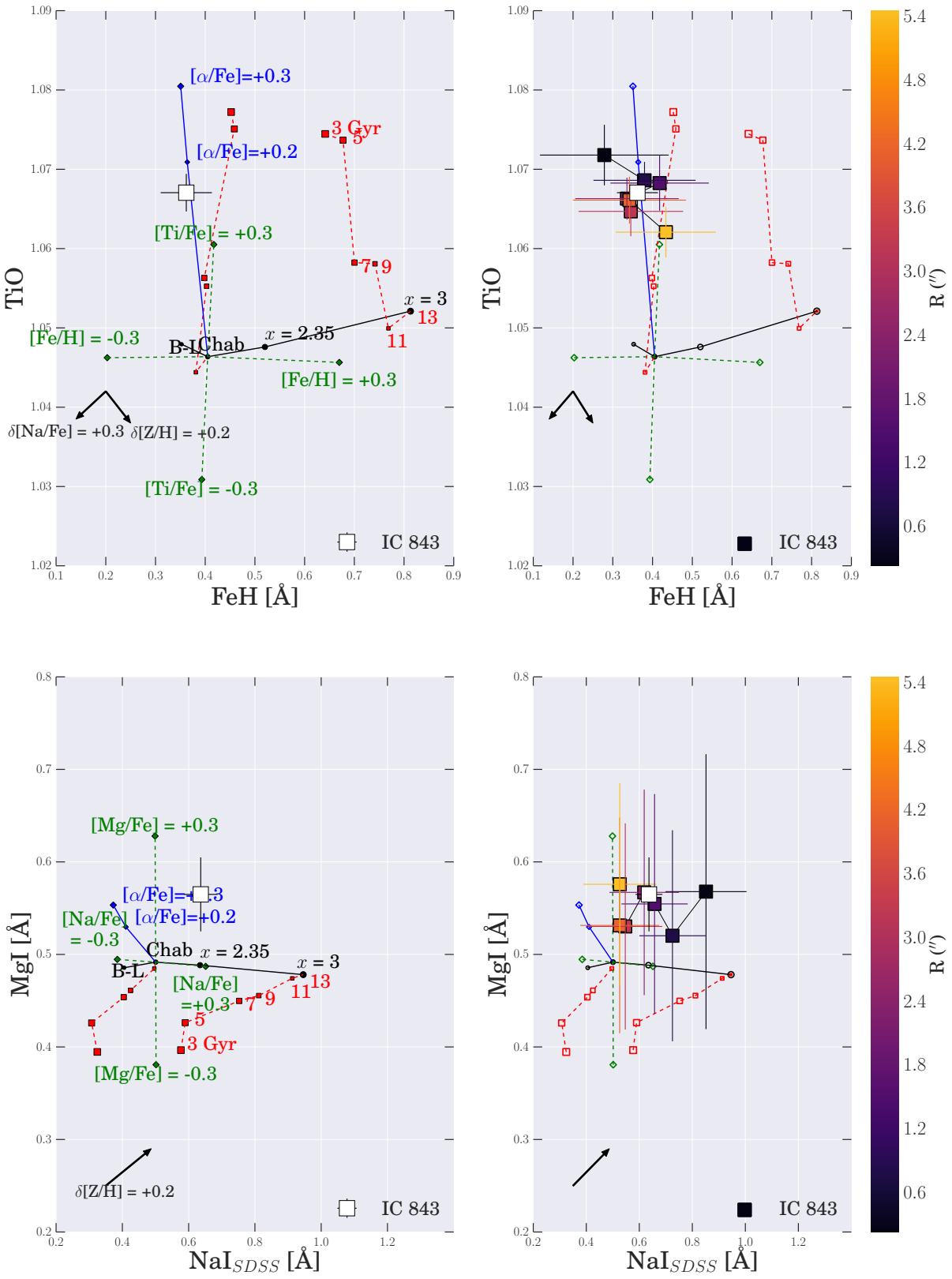

Figure 7. As Figure 6, but for IC 843. We infer a Chabrier IMF in a +0.2 [α/Fe] enhanced population with an enhancement in [Na/Fe] (see Section 5.4 for details).

side the parameter space spanned by the CvD12 models, we turn to the Na-MILES models of La Barbera et al. (2016a). These are SSP models based on the extended MILES models of Röck et al. (2016), with enhancements in [Na/Fe] of up to 1.2 dex at a range of metallicities, bimodal IMF slopes and ages. In Figure 8 we plot a map of NaI_{SDSS} against MgI for these Na enhanced models.

We choose population parameters from the Na-Miles models to closely match those measured in NGC 1277; namely [Z/H]=+0.22 and an age of 14.125 Gyr. However, the Na-MILES models are computed at solar alpha abundance, which isn't appropriate for NGC 1277. Taking the CvD12 spectra, we create a linear response function from the [α/Fe]=0.0 and +0.3 spectra with Chabrier IMFs and apply it to the Na-MILES models to account for the α-enhancement measured in this object. This is discussed in Appendix B.

The data and model grids are shown in Figure 8. The diamond points vary from [Na/Fe]=+0.0 (blue) to [Na/Fe]=0.9 (red), with each point representing the location of a Chabrier (Γ_b=1.3) IMF. Data points are coloured from dark (centre) to light (outskirts) with the same colours as Figure 6.

Figure 8 shows that, unlike for the CvD12 SSP models, our NaI_{SDSS} measurements in NGC 1277 fall well within the parameter space of Na-MILES. Interpolation of the Chabrier IMF points lead to a [Na/Fe] enhancement of +0.5 dex in the global, luminosity weighted spectrum and a [Na/Fe] gradient of 0.23 dex kpc^{-1}. [1]. The strength of the NaI_{SDSS} measurements may be due to contamination from the interstellar medium, although no dust lanes are visible in this object. We note that MN15 measure an even stronger NaI_{SDSS} gradient in NGC 1277 than observed here, with their NaI_{SDSS} points dropping from >1.4Å in the centre to 0.9Å at 1.5 R_e (their Figure 3).

With these caveats in mind, we therefore conclude that NGC 1277 is an old, alpha enhanced population with a Chabrier-like IMF slope and steep gradient in [Na/Fe].

5.4 IC 843

Figure 7 shows the same index-index maps for IC 843. The TiO-FeH results scatter around a +0.2 [α/Fe] enhanced Chabrier IMF, marginally consistent with the [α/Fe] enhancement derived from optical indices. The slight radial trend in the TiO measurements could be explained by a trend in α-enhancement. As for NGC 1277, the global spectrum is inconsistent with a bottom heavy unimodal IMF.

Whilst the MgI-NaI_{SDSS} plot could be read as implying an IMF slope of $x > 3$ in the centre, which reduces to $x \sim 2.5$ in the outskirts, an enhancement of [Na/Fe] would also explain the strength of the NaI line. Similarly to the case for NGC 1277 we conclude a gradient in [Na/Fe] instead of an IMF gradient, due to the measured strength of FeH and lack of evidence for [Fe/H] under-abundance in the optical index measurements. From interpolation of Figure 8, the upper limit to the [Na/Fe] abundance measured from the global spectrum and the Na-MILES models is +0.2 dex, with a gradient of 0.15 dex kpc^{-1}. The central point corresponds to an enhancement in [Na/Fe] of +0.44 dex, whilst the outermost points has [Na/Fe]=0.0.

These index measurements lead us to conclude that IC 843 has a Chabrier-like IMF slope in an old population, with a similar α-enhancement to NGC 1277 but smaller overall enhancement in [Na/Fe].

6 DISCUSSION

6.1 Tension between IMF-sensitive indices

Both our galaxies show strong gradients in NaI absorption but FeH profiles which are flat with radius. This behaviour may seem surprising, since both indices are found to be IMF sensitive: i.e. strong in low-mass dwarf stars but not in low-mass giants. Naively, a change in the low mass IMF slope would cause both indices to increase or decrease simultaneously.

Whilst it is true that the Wing-Ford band and NaI are both caused by absorption in the atmospheres of dwarf stars, each is strongest in stars of a slightly different mass. FeH is more sensitive than NaI to stars below around 0.2 $M_\odot$, whereas NaI is stronger at 0.2 $M_\odot$< M < 0.6 $M_\odot$ (Conroy & van Dokkum 2012, Figure 17). The radial behaviour of both indices could be explained by an IMF which is constant with radius below 0.2 $M_\odot$ yet varies sharply as a function of radius at M $\gtrsim$ 0.4 $M_\odot$, but such a scenario demands extraordinary changes in the numbers of dwarf stars (of very specific masses) on sub-kpc scales.

We conclude in favour of [Na/Fe] over-abundance in these objects, which acts to mimic the effect of an IMF gradient, for a number of reasons. Previous work has raised questions over the use of sodium features to determine IMF slope. Smith et al. (2015b) caution against the use of sodium indices in spectroscopic determination of the IMF, whilst Conroy & van Dokkum find that far red sodium indices cannot be used to both constrain the IMF slope and [Na/Fe] abundance ratios, since they respond in the same way to both effects.

Furthermore, Jeong et al. (2013) find excess NaD strengths in ∼8% of low redshift ($z < 0.08$) SDSS DR7 galaxies, including in ETGs without visible dust lanes. They conclude that [Na/Fe] enhancement, rather than ISM or IMF effects, are the cause. Both Worthey et al. (2014) and Conroy et al. (2014) also find a trend of increasing [Na/Fe] abundance in galaxies with larger velocity dispersions, of up to ∼ 0.4 dex in galaxies with σ=300 kms^{-1}, using independent SPS models. Their measured [Na/Fe] over-abundances are perfectly consistent with the abundances estimated here of +0.2 dex in IC 843 (σ_0 = 265 kms^{-1}) and +0.5 dex in NGC 1277 (σ_0 = 410 kms^{-1}). Super solar [Na/Fe] abundance ratios are therefore not uncommon in massive ETGs.

Our conclusion relies, however, on our interpretation of the strength of the Wing-Ford band being correct: could a similar abundance gradient be suppressing the FeH absorption strength and masking a bottom heavy IMF? Possible iron abundance variations can be easily constrained by optical indices such as Fe52 and/or Fe53 (Conroy & van Dokkum

[1] Note that these values are upper limits on the [Na/Fe] abundance ratio. The Na-MILES models are computed assuming Local Thermodynamical Equilibrium (LTE), which may not be appropriate for transitions involving NaI in late type stars: see Section 9 of La Barbera et al. (2016a)

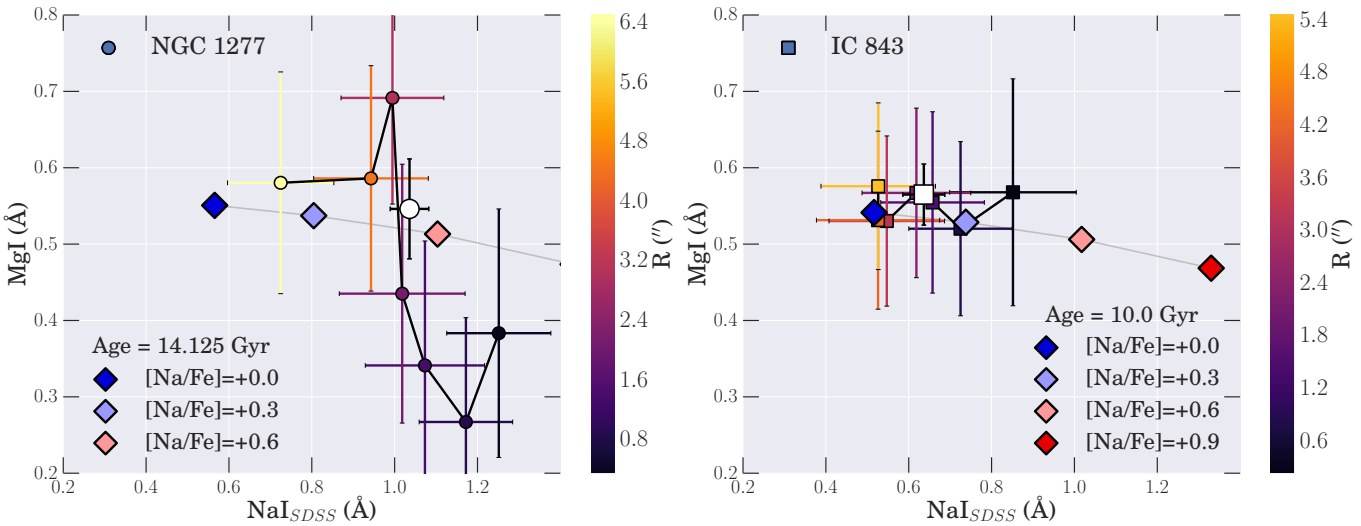

Figure 8. Plots of NaI$_{\rm SDSS}$ against MgI for NGC 1277 (left) and IC 843 (right), with model lines from the Na-MILES models (La Barbera et al. 2016a; Röck et al. 2016). Diamonds are coloured from blue ([Na/Fe]=+0.0) to red ([Na/Fe]=+0.9), with each diamond representing the location of a Chabrier IMF (Γ_b=1.3). We fix the other parameters of the model to be [Z/H]=+0.22 and [α/Fe]=+0.3 for both galaxies, and age as labelled on each plot. Note that the Na-MILES model spectra are all computed at solar [α/Fe], and so we have used response functions from the CvD12 models to correct them to [α/Fe]=+0.3 (see Appendix B). By assuming a Chabrier IMF in both objects, we use this plot to find an upper limit for the enhancement in [Na/Fe] in both NGC 1277 and IC 843.

2012), and we see no evidence for a low [Fe/H] ratio in either NGC 1277 or IC 843. The production and abundance ratios of iron and hydrogen have been well studied and understood for decades (e.g. Faber 1983; Worthey et al. 1994; Trager et al. 1998), and measuring an [Fe/H] under-abundance of $\sim$ 0.3 dex in either of these massive ETGs would be very surprising. FeH is also relatively insensitive to [α/Fe] enhancement and age gradients (Conroy & van Dokkum 2012).

Our flat FeH profiles may seem surprising in one sense, however. Both the CvD12 and Na-MILES model show that FeH is strengthened by increased [Z/H], and metallicity gradients are common in ETGs: indeed, the radial measurements of optical indices show evidence for a metallicity gradient in NGC 1277. However, both sets of models also show that enhanced [Na/Fe] tends to weaken the strength of FeH. This effect comes from the complex interplay between different molecules in the atmospheres of the stars in each galaxy. Na is an important electron contributor in late-type giants and dwarfs, which weakens the equivalent width of molecules like the CaT and the Wing Ford band. The two second order effects of [Z/H] and [Na/Fe] therefore work in opposite directions and tend to cancel each other out, and so our conclusions of [Na/Fe] gradients help to explain why our FeH measurements show no radial change when one might be expected.

6.2 Radial IMF slope measurements

Following Zieleniewski et al. (2016), we derive unimodal IMF slopes from our index measurements. Using the age of each galaxy from section 5.1, we interpolate the CvD12 models to find SSPs at varying IMF at a given age. The FeH index values of these models are then compared to our FeH measurements, and a unimodal IMF slope calculated. 1-σ uncertainties are propagated from our measurement uncertainties.

Figure 9 shows our IMF slope measurements against radius for both NGC 1277 (blue) and IC 843 (red). We have investigated the use of response functions to account for variations in [α/Fe], [Fe/H] and [Na/Fe] from solar abundance patterns in both galaxies, and found them to have very small effects at all radii. A further discussion of the details of such response functions is saved for Appendix B, as well as a plot of the IMF slope measurement against radius which includes these corrections.

Our measurements are consistent with a Chabrier-like IMF in both objects. There is slight evidence for a steepening of the IMF slope with radius in NGC 1277, but further investigation would be required to confirm this. A unimodal IMF more bottom heavy than Salpeter is rejected for both galaxies.

FeH is most sensitive to the lowest mass stars in a galaxy (M$<$ 0.2 M$_\odot$). Our results imply that the low-mass end of the IMF slope is the same at all radii in these galaxies, and that the low-mass end closely resembles that of a Chabrier (i.e. bimodal) IMF. This qualitatively agrees with the findings of MN15, who use a bimodal parameterisation of the IMF at all radii in NGC 1277.

MN15 measure a gradient in the high-mass IMF slope in NGC 1277, from Γ_b=3 in the centre to Γ_b=2.5 at 1.2 R$_e$. Constraining the high-mass index of a bimodal IMF using the Wing-Ford band is difficult, although not impossible. Changing the high-mass slope of the IMF also requires a change in IMF normalisation to ensure that the integral over all masses still results in the total mass of the galaxy. As such, the proportion of low mass stars, and hence FeH feature strength, changes slightly between bimodal IMFs with different Γ_b.

An initial analysis of the global luminosity-weighted FeH measurement in NGC 1277 shows it is $\sim 1.8\sigma$ away from the value expected in an old, alpha-enhanced, metal-rich population with the bottom-heavy bimodal IMF of Γ_b=3.0

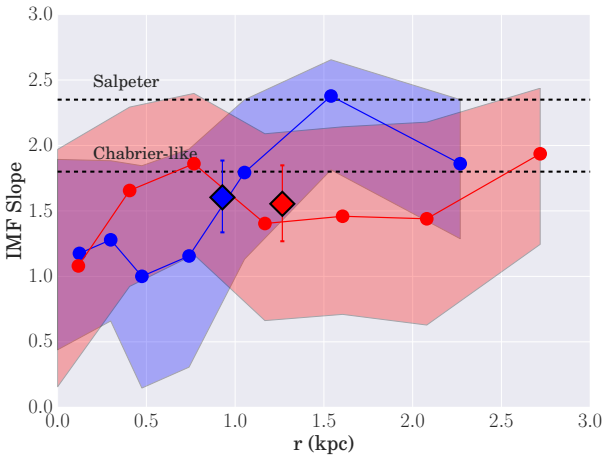

Figure 9. Unimodal IMF slope against radius for NGC 1277 (blue) and IC 843 (red). Diamonds correspond to IMF slope found using the global measurement in each galaxy. Shaded regions show 1-σ uncertainties. The measured FeH equivalent width leads to Chabrier-like unimodal IMFs at all radii in both galaxies, with only marginal evidence for an IMF gradient in the outskirts of NGC 1277. See section 6.2 for details.

found by MN15, but further investigation is required to confirm this. Future work will explore the use of our all of measurements, combined with the Na-MILES models and previously published data, to study a bimodal parameterisation of the IMF slope as a function of radius in both these objects.

6.3 Proposed IMF correlations

Figure 10 shows *global* IMF slopes of the galaxies studied in this work, as well as measurements of global IMF slopes in Coma BCGs from Zieleniewski et al. (2016). Our IMF slope measurements are derived from our global FeH measurements in both galaxies. As in section 6.2, we again find that corrections for non-solar [α/Fe], [Fe/H] and [Na/Fe] abundance values are small. Appendix B shows an identical plot to Figure 10, but including these response functions.

Many authors (e.g. Ferreras et al. 2013; La Barbera et al. 2013b; Spiniello et al. 2014) have found trends of increasing global unimodal IMF slope with galaxy velocity dispersion, in that more massive ETGs with larger σ_0 tend to have a unimodal IMF slope which is more bottom heavy than the Milky Way. The relationships differ slightly, but generally galaxies with σ_0>200 kms^{-1} have IMF slopes heavier than Salpeter (σ_0>250 kms^{-1} for S14) whilst galaxies with σ_0<150 kms^{-1} have Chabrier-like IMFs. Figure 10 includes three proposed IMF-Sigma relationships.

We find that four out of five galaxies with σ_0>250 kms^{-1}, spanning a variety of environments, ages and sizes, are inconsistent with these relations. Further investigation is required to understand these discrepancies. We also find, in agreement with MN15, that local velocity dispersion cannot be a driving force for IMF gradients. Both objects in this study exhibit peaked σ profiles in their centres with no comparable gradient in FeH equivalent width or IMF slope.

6.4 Other radial studies of FeH and NaI

Similar results and conclusions to ours have been reached by other authors who have measured both NaI and FeH as a function of radius in a variety of objects. Zieleniewski et al. (2015) studied the central bulge of M31, observing a large decrease in NaI combined with no radial change in FeH, and conclude in favour of a gradient in [Na/Fe] rather than the IMF. Furthermore, Zieleniewski et al. (2016) studied the brightest cluster galaxies (BCGs) in the Coma cluster, measuring a strong gradient in NaI combined with flat FeH profile in the massive ETG NGC 4889, which has a central velocity dispersion of nearly 400 kms^{-1}. Other objects in the sample also show weak FeH absorption. Only NGC 4839 displays evidence for a deep Wing-Ford band, although large systematic uncertainty due to residual sky emission prevents the authors from drawing strong conclusions about its stellar population.

McConnell et al. (2016) obtained deep long-slit data on two nearby ETGs, both of which had been part of the van Dokkum & Conroy (2012) sample. They found strong gradients in NaI but a much weaker decline in FeH, as well as opposite behaviour in NaI/$\langle$Fe$\rangle$ and FeH/$\langle$Fe$\rangle$. Again, the authors conclude in favour of a variation in [Na/Fe] over the central $\sim$300 pc of each galaxy instead of the IMF driving the strong decline in NaI. The authors also argue, as we do, that the flat FeH profile implies a fixed low-mass slope of the IMF below M<$\sim$ 0.4$M_{\odot}$.

Finally, La Barbera et al. (2016a) use the Na-MILES models to infer a bimodal IMF gradient *as well as* a gradient in [Na/Fe] in a nearby ETG, by measuring NaI, NaD and two further Na lines at 1.14 and 2.21 μm. Discussion of further optical and far red lines in the same galaxy are presented La Barbera et al. (2016b), where the authors measure no radial gradient in FeH. This work is only possible due to the huge parameter space spanned by the Na-MILES SSP models, which are a very impressive accomplishment.

The Na-MILES models use the bimodal IMF form of Vazdekis et al. (1996), which uses a spline interpolation between the varying high-mass slope and fixed low-mass end below 0.2 M$_{\odot}$. This spline is exactly between the stellar mass region where the NaI line is strongest, and an interesting avenue of future work would be to see how robust the utility of Na lines is to sensible changes in IMF parametrization. For example, an IMF model with a fixed low mass form up to 0.6 M$_{\odot}$ (instead of 0.2 M$_{\odot}$) would tie the IMF response of the very low mass indicators (such as FeH and NaI1.14) to the IMF response of the NaI line at 8190Å. With such a form of the IMF, seeing a gradient in the Na lines but not FeH would unquestionably be due to abundance gradients. Whilst creating SSP templates for huge numbers of different IMF shapes would not be a useful exercise, we do believe that further investigation of the precise details of the bimodal IMF is warranted.

7 CONCLUSIONS

We have used the Oxford SWIFT instrument to undertake a study of two low redshift galaxies in order to make resolved measurements of their IMF slope. We obtained high S/N integral field data of NGC 1277, a fast rotator in the

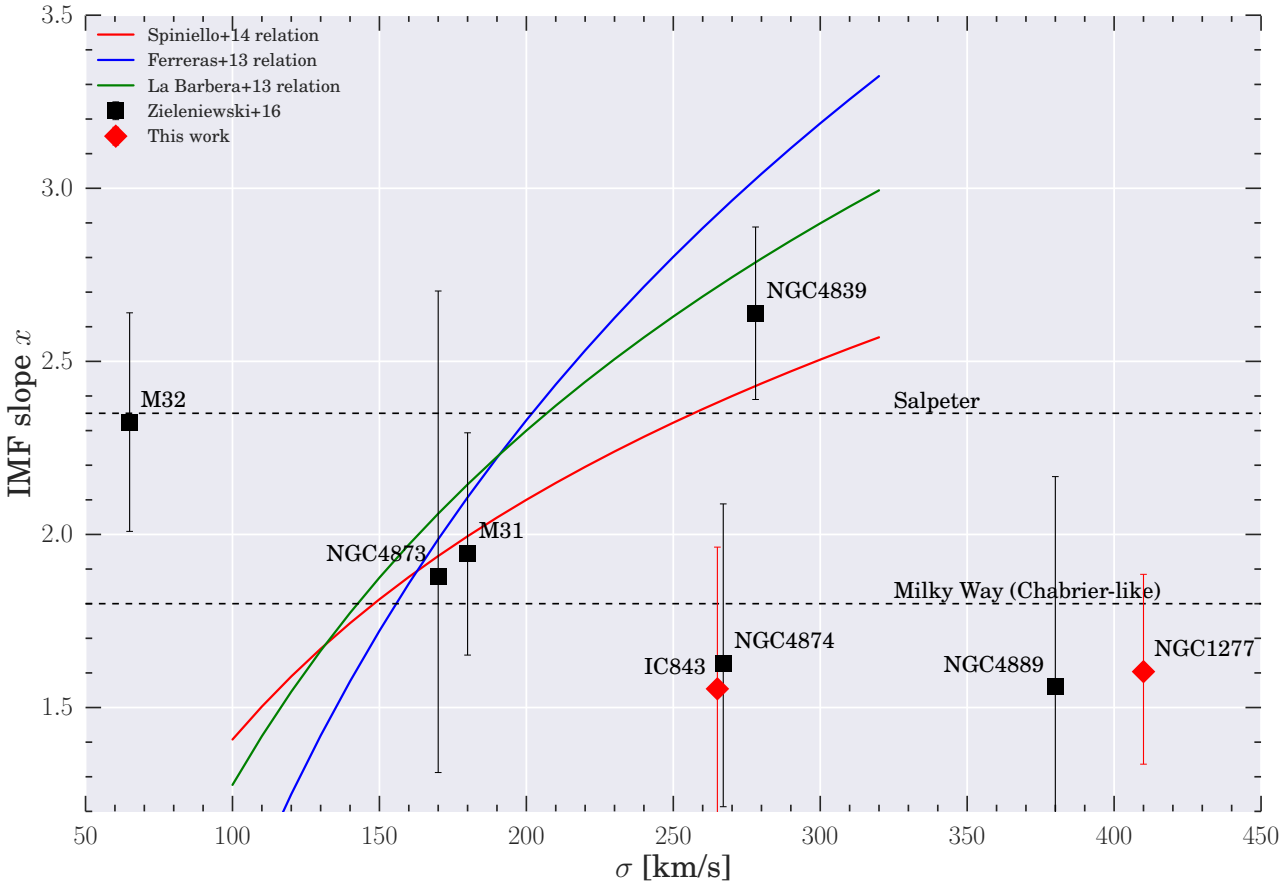

Figure 10. Unimodal IMF slope against velocity dispersion for the galaxies studied in this work, Zieleniewski et al. (2015) and Zieleniewski et al. (2016). Coloured lines show proposed IMF-σ relationships from Spiniello et al. (2014), Ferreras et al. (2013) and La Barbera et al. (2013b). Four out of five galaxies with σ_0>250 kms^{-1} lie away from these relationships.

Perseus cluster with a very high central velocity dispersion, and IC 843, also a fast rotator, located in the Coma cluster. Our measurements extend out to 7.7″ and 6.2″ respectively, corresponding to 2.2 and 0.65 R_e. The SWIFT wavelength coverage, from 6300 Å to 10412 Å, allows radial measurement of the NaI doublet, CaII triplet, TiO, MgI and FeH absorption features, which we compare to stellar population models from van Dokkum & Conroy (2012). We conclude:

(i) NGC 1277 shows a strong negative gradient in NaI, slight negative TiO and CaT gradients and flat FeH and MgI profiles. The FeH equivalent widths are low, at around 0.35-0.4 Å at all radii. Comparisons to stellar population models and previous work using optical indices lead us to infer a unimodal Chabrier-like IMF slope at all radii in an old, [α/Fe] enhanced population with a strong abundance gradient in [Na/Fe].

(ii) IC 843 is similar, if less extreme, than NGC 1277. It displays a weaker NaI$_{\rm SDSS}$ gradient and flat profiles in FeH, TiO, CaT and MgI. FeH equivalent widths are slightly higher than in NGC 1277 at around 0.4 Å. We again find evidence for a unimodal Chabrier-like IMF slope at all radii, in an old population with [α/Fe]$\sim$+0.3 dex and an enhancement in [Na/Fe].

(iii) Similarly to McConnell et al. (2016) and Zieleniewski et al. (2016), we find strong disagreement between the IMF sensitive indices NaI and FeH. We use the Na-MILES models (La Barbera et al. 2016a) to explain the anomalous strength of NaI absorption in NGC 1277 and IC 843 as a global [Na/Fe] enhancement of up to +0.5 dex and +0.2 dex respectively.

(iv) In both NGC 1277 and IC 843, we conclusively rule out unimodal IMF slopes more bottom heavy than Salpeter at all radii.

(v) Both galaxies are in tension with the unimodal IMF-σ relationships found by Ferreras et al. (2013), La Barbera et al. (2013b) and Spiniello et al. (2014). Most strikingly, NGC 1277 has a central velocity dispersion of 410 kms^{-1} yet we measure the same unimodal IMF slope as predicted in a galaxy with σ_0 $\sim$150 kms^{-1}.

Of the galaxies studied in Zieleniewski et al. (2015), Zieleniewski et al. (2016) and in this work, none have shown evidence of radial gradients in FeH or any large departure from an equivalent width of $\sim$ 0.4Å, even when other line strengths vary wildly. Such consistency between different objects is most simply explained by a parameter being the same in each galaxy, and this parameter could well be the low-mass slope of the IMF.

ACKNOWLEDGEMENTS

SPV would like to thank F. La Barbera for making available the Na-MILES models used in this paper, and P. Alton for fruitful discussions on the effect of Na on stellar atmospheres.

This paper made heavy use of the Astropy python packages (Astropy Collaboration et al. 2013) and `seaborn` plotting software (Waskom et al. 2015).

The Oxford SWIFT integral field spectrograph was supported by a Marie Curie Excellence Grant from the European Commission (MEXT-CT-2003-002792, Team Leader: N. Thatte). It was also supported by additional funds from the University of Oxford Physics Department and the John Fell OUP Research Fund. Additional funds to host and support SWIFT at the 200-inch Hale Telescope on Palomar were provided by Caltech Optical Observatories.

This work was supported by the Astrophysics at Oxford grants (ST/H002456/1 and ST/K00106X/1) as well as visitors grant (ST/H504862/1) from the UK Science and Technology Facilities Council. SPV is supported by a doctoral studentship supported by STFC grant ST/N504233/1. RCWH was supported by the Science and Technology Facilities Council [STFC grant numbers ST/H002456/1, ST/K00106X/1 & ST/J002216/1]. RLD acknowledges travel and computer grants from Christ Church, Oxford, and support from the Oxford Centre for Astrophysical Surveys, which is funded through generous support from the Hintze Family Charitable Foundation.

References

Anderson T. W., Darling D. A., 1954, Journal of the American Statistical Association, 49, 765
Astropy Collaboration et al., 2013, A&A, 558, A33
Bastian N., Covey K. R., Meyer M. R., 2010, ARA&A, 48, 339
Cappellari M., Emsellem E., 2004, Publications of the Astronomical Society of the Pacific, 116, 138
Cappellari M., et al., 2011, MNRAS, 413, 813
Cappellari M., et al., 2013, MNRAS, 432, 1862
Cenarro A. J., Cardiel N., Gorgas J., Peletier R. F., Vazdekis A., Prada F., 2001, MNRAS, 326, 959
Cenarro A. J., Gorgas J., Vazdekis A., Cardiel N., Peletier R. F., 2003, MNRAS, 339, L12
Chabrier G., 2003, PASP, 115, 763
Clauwens B., Schaye J., Franx M., 2016, MNRAS, 462, 2832
Clough S. A., Shephard M. W., Mlawer E. J., Delamere J. S., Iacono M. J., Cady-Pereira K., Boukabara S., Brown P. D., 2005, J. Quant. Spectrosc. Radiative Transfer, 91, 233
Cohen J. G., 1978, ApJ, 221, 788
Conroy C., van Dokkum P., 2012, ApJ, 747, 69
Conroy C., Graves G. J., van Dokkum P. G., 2014, ApJ, 780, 33
Couture J., Hardy E., 1993, ApJ, 406, 142
Davies R. I., 2007, MNRAS, 375, 1099
Emsellem E., 2013, MNRAS, 433, 1862
Faber S. M., 1983, Highlights of Astronomy, 6, 165
Faber S. M., French H. B., 1980, Lick Observatory Bulletin, 823, 1
Ferreras I., La Barbera F., de la Rosa I. G., Vazdekis A., de Carvalho R. R., Falcón-Barroso J., Ricciardelli E., 2013, MNRAS, 429, L15
Hopkins P. F., Bundy K., Murray N., Quataert E., Lauer T. R., Ma C.-P., 2009, MNRAS, 398, 898
Jeong H., Yi S. K., Kyeong J., Sarzi M., Sung E.-C., Oh K., 2013, ApJS, 208, 7
Kausch W., et al., 2014, in Manset N., Forshay P., eds, Astronomical Society of the Pacific Conference Series Vol. 485, Astronomical Data Analysis Software and Systems XXIII. p. 403 (arXiv:1401.7768)
Korn A. J., Maraston C., Thomas D., 2005, A&A, 438, 685
Kroupa P., 2001, MNRAS, 322, 231
La Barbera F., Ferreras I., Vazdekis A., de la Rosa I. G., de Carvalho R. R., Trevisan M., Falcón-Barroso J., Ricciardelli E., 2013a, MNRAS, 433, 3017
La Barbera F., Ferreras I., Vazdekis A., de la Rosa I. G., de Carvalho R. R., Trevisan M., Falcón-Barroso J., Ricciardelli E., 2013b, MNRAS, 433, 3017
La Barbera F., Vazdekis A., Ferreras I., Pasquali A., Allende Prieto C., Rock B., Aguado D. S., Peletier R. F., 2016a, preprint, (arXiv:1610.03853)
La Barbera F., Vazdekis A., Ferreras I., Pasquali A., Cappellari M., Martín-Navarro I., Schönebeck F., Falcón-Barroso J., 2016b, MNRAS, 457, 1468
Martín-Navarro I., Barbera F. L., Vazdekis A., Falcón-Barroso J., Ferreras I., 2015a, MNRAS, 447, 1033
Martín-Navarro I., La Barbera F., Vazdekis A., Ferré-Mateu A., Trujillo I., Beasley M. A., 2015b, MNRAS, 451, 1081
Martín-Navarro I., et al., 2015c, ApJ, 806, L31
McConnell N. J., Lu J. R., Mann A. W., 2016, ApJ, 821, 39
Naab T., Johansson P. H., Ostriker J. P., 2009, ApJ, 699, L178
Price J., Phillipps S., Huxor A., Smith R. J., Lucey J. R., 2011, MNRAS, 411, 2558
Röck B., Vazdekis A., Ricciardelli E., Peletier R. F., Knapen J. H., Falcón-Barroso J., 2016, A&A, 589, A73
Salpeter E. E., 1955, ApJ, 121, 161
Schiavon R. P., Barbuy B., Rossi S. C. F., Milone A. 1997a, ApJ, 479, 902
Schiavon R. P., Barbuy B., Singh P. D., 1997b, ApJ, 484, 499
Smith R. J., 2014, MNRAS, 443, L69
Smith R. J., Lucey J. R., Conroy C., 2015a, MNRAS, 449, 3441
Smith R. J., Alton P., Lucey J. R., Conroy C., Carter D., 2015b, MNRAS, 454, L71
Spiniello C., Trager S., Koopmans L. V. E., Conroy C., 2014, MNRAS, 438, 1483
Spiniello C., Barnabè M., Koopmans L. V. E., Trager S. C., 2015, MNRAS, 452, L21
Thatte N., Tecza M., Clarke F., Goodsall T., Lynn J., Freeman D., Davies R. L., 2006, in Society of Photo-Optical Instrumentation Engineers (SPIE) Conference Series. p. 62693L, doi:10.1117/12.670859
Thomas D., Maraston C., Bender R., Mendes de Oliveira C., 2005, ApJ, 621, 673
Thomas J., Saglia R. P., Bender R., Thomas D., Gebhardt K., Magorrian J., Corsini E. M., Wegner G., 2007, MNRAS, 382, 657
Thomas D., Maraston C., Johansson J., 2011a, MNRAS, 412, 2183
Thomas J., et al., 2011b, MNRAS, 415, 545
Trager S. C., Worthey G., Faber S. M., Burstein D., González J. J., 1998, ApJS, 116, 1
Trager S. C., Faber S. M., Worthey G., González J. J., 2000, AJ, 120, 165
Treu T., Auger M. W., Koopmans L. V. E., Gavazzi R., Marshall P. J., Bolton A. S., 2010, ApJ, 709, 1195
Trujillo I., Ferré-Mateu A., Balcells M., Vazdekis A., Sánchez-Blázquez P., 2014, ApJ, 780, L20
Vazdekis A., Casuso E., Peletier R. F., Beckman J. E., 1996, ApJS, 106, 307
Vazdekis A., et al., 2015, MNRAS, 449, 1177
Waskom M., et al., 2015, seaborn: v0.6.0 (June 2015), doi:10.5281/zenodo.19108, https://doi.org/10.5281/zenodo.19108
Weijmans A.-M., et al., 2009, MNRAS, 398, 561

Wing R. F., Ford Jr. W. K., 1969, PASP, 81, 527
Worthey G., Faber S. M., Gonzalez J. J., Burstein D., 1994, ApJS, 94, 687
Worthey G., Tang B., Serven J., 2014, ApJ, 783, 20
Zieleniewski S., Houghton R. C. W., Thatte N., Davies R. L., 2015, MNRAS, 452, 597
Zieleniewski S., Houghton R. C. W., Thatte N., Davies R. L., Vaughan S. P., 2016, preprint, (arXiv:1611.01095)
van Dokkum P. G., 2001, PASP, 113, 1420
van Dokkum P. G., 2008, ApJ, 674, 29
van Dokkum P. G., Conroy C., 2010, Nature, 468, 940
van Dokkum P. G., Conroy C., 2012, ApJ, 760, 70
van den Bosch R. C. E., Gebhardt K., Gültekin K., van de Ven G., van der Wel A., Walsh J. L., 2012, Nature, 491, 729

APPENDIX A: SKY SUBTRACTION METHODS

First order sky subtraction was applied to each galaxy cube. This involved subtracting a separate "sky" cube, made by combining sky observations taken throughout the night, from the combined galaxy data. Since night sky emission lines vary with a timescale of order minutes, similar in length to our observations, the resulting sky subtracted spectra still contain residual sky light. To subtract this residual sky emission, we use `pPXF` to fit a set of sky templates at the same time as we measure the kinematics from each spectrum, a process first described in Weijmans et al. (2009).

The sky templates are made from the sky cube used for first order sky subtraction. The observed sky spectrum is split around selected molecular bandheads and transitions, according to wavelengths defined in Davies (2007), so that emission lines corresponding to different molecules are allowed to be scaled separately in `pPXF`. A small number of further splits were introduced by finding where sky residuals were seen to sharply change sign. We also allow for over-subtracted skylines by including negatively scaled sky spectra. A full sky spectrum with locations of sky splits marked is shown in Figures A1 and A2.

The area worst affected by residual sky emission is the Wing-Ford band at 9916 Å. Here, we found that changing the combination of sky splits had an impact on the quality of sky subtraction, and hence on the FeH equivalent width measurement. To quantitatively choose the set of skyline splits which gave us the best sky subtraction, we investigated the residuals of the sky subtracted spectrum around the best fitting `pPXF` template. Any remaining skylines which weren't subtracted well by `pPXF` will lead to outlying residuals around a Gaussian distribution. A set of residuals which have tails which deviate from a normal distribution therefore imply a poor sky subtraction.

Around FeH, there are 5 wavelengths which we decided to split the sky at; 9933 Å, 10054 Å, 10094 Å, 1013 9Å and 1.01865 Å. This leads to $2^5 = 32$ possible combinations of splits. We investigated the residuals for each of these 32 combinations, both by eye and using an Anderson-Darling test (Anderson & Darling 1954, AD) with the null hypothesis that each sample was drawn from a normal distribution. The AD test is very similar to the more commonly used Kolmogorov-Smirnov test, except with a weighting function which emphasises the tails of each distribution more than a KS test otherwise would. For all analysis in this work we used the selection of sky splits with the lowest AD statistic, which corresponds to the residual distribution best described by a normal distribution with no outliers. A plot of the best (green) and worst (red) residual distribution for the NGC 1277 skylines is shown in Figure A3, whilst Figure A4 shows our FeH spectra for NGC 1277 and IC 843 before and after second order sky subtraction. The spectra which, by eye, have the best sky subtraction are also those with the lowest AD statistic.

A0.1 Independent Sky Subtraction Methods Comparison

Figure A5 shows equivalent width measurements of the Wing Ford band, found using spectra from the two sky subtraction processes; subtracting skylines with `pPXF` and median profile fitting. Both methods are described in Section 3.1.

The two methods show good agreement, showing that our FeH measurements are robust despite the challenging nature of removing residual sky emission in the far red region of the spectrum.

APPENDIX B: RESPONSE FUNCTIONS

In order to make quantitative measurements of the IMF in each galaxy, we interpolate the base set of CvD12 models of varying IMF slope as a function of age and FeH equivalent width. These base spectra are at solar metallicity, [α/Fe]=0 and have solar abundance ratios whilst spanning IMF slopes from bottom-light to $x = 3.0$. To accurately account for the different metallicities, α-abundances and [Na/Fe] ratios in each galaxy, we apply linear response functions to the CvD spectra.

The first order correction is defined as follows. To deal with varying continuum levels between spectra with different IMF slopes, we use multiplicative rather than additive response functions. For a spectrum with a non-solar α-abundance ratio, $S(\Delta\alpha)$,

$$S(\Delta\alpha) = x_\alpha S(\Delta\alpha = 0.0) \tag{B1}$$

$$= S(\Delta\alpha = 0.0) + \frac{dS}{d\alpha}\Delta\alpha \tag{B2}$$

$$x_\alpha = (1 + \frac{d\ln S}{d\alpha}\Delta\alpha) \tag{B3}$$

We approximate the gradient term using a model spectrum from CvD12 at enhanced [α/Fe]=+0.3 to give

$$\frac{d\ln S}{d\alpha}\Delta\alpha \approx \frac{1}{S(\Delta\alpha = +0.0)} \frac{S(\Delta\alpha = +0.3) - S(\Delta\alpha = +0.0)}{10^{0.3} - 1}(10^{\Delta\alpha} - 1) \tag{B4}$$

$$= \left(\frac{S(\Delta\alpha = +0.3)}{S(\Delta\alpha = +0.0)} - 1\right) \frac{10^{\Delta\alpha} - 1}{10^{0.3} - 1} \tag{B5}$$

$$= f_\alpha \tag{B6}$$

A similar correction is applied for [Na/Fe] and [Fe/H] abundance variations. This means the final set of spectra are:

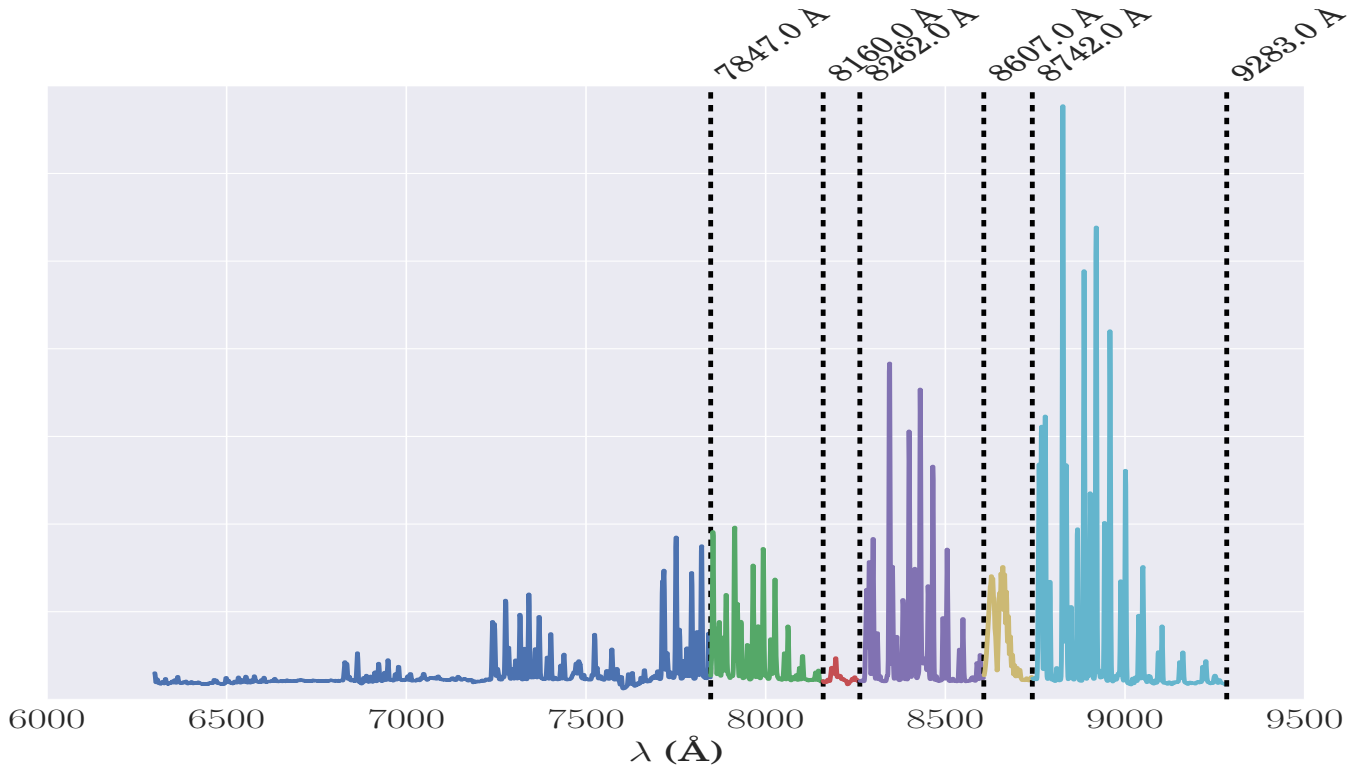

Figure A1. A sky spectrum from 6300 Å to 9283 Å, showing locations of split locations.

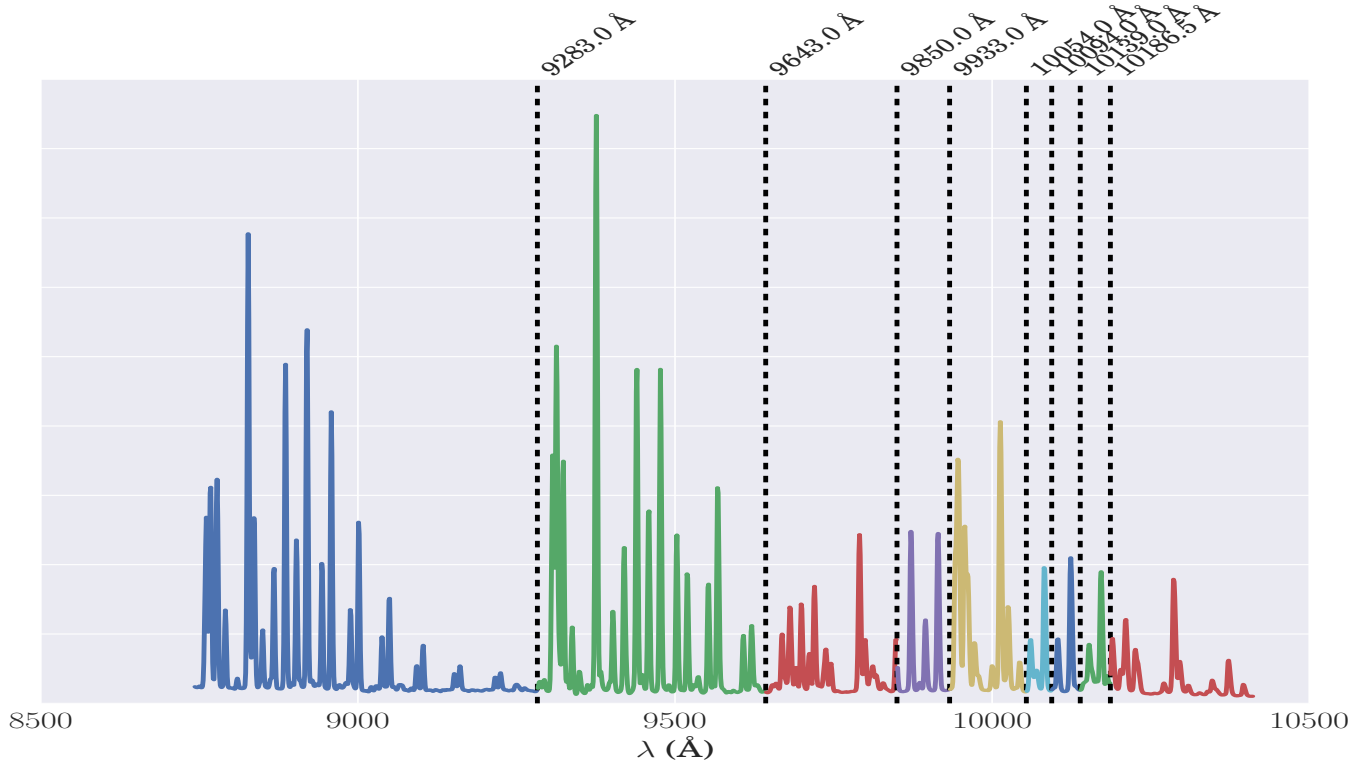

Figure A2. A sky spectrum centred around the Wing Ford band, showing the locations of sky splits. At the redshift of NGC 1277 and IC 843, the Wing-Ford band is observed at 10085 Å and 10160 Å respectively.

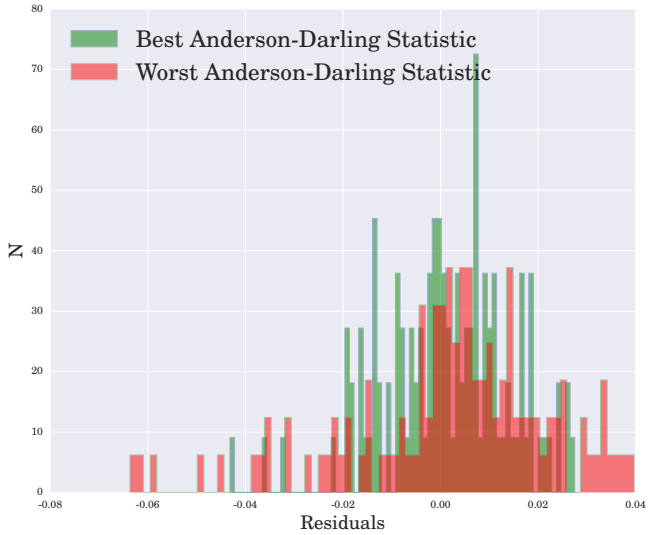

Figure A3. NGC 1277 residuals of two sets of sky line splits around the best fit `pPXF` template, after second order sky subtraction. The histogram in green shows the distribution with the lowest Anderson-Darling test statistic of all 32 sky split combinations, whilst the one in red shows a distribution with many outlying residuals and a large A-D statistic, corresponding to a poor second-order sky subtraction.

$$S_{\rm final} = S_0 \cdot x_\alpha \cdot x_{\rm Na} \cdot x_{\rm Fe} \tag{B7}$$

$$\ln S_{\rm final} = \ln S_0 + f_\alpha + f_{\rm Na} + f_{\rm Fe} \tag{B8}$$

The changes these response functions lead to are small and make no difference to our conclusions. Figure B1 shows the changes to Figure 9 when including response functions, whilst Figure B2 does the same for Figure 10

This paper has been typeset from a TEX/LATEX file prepared by the author.

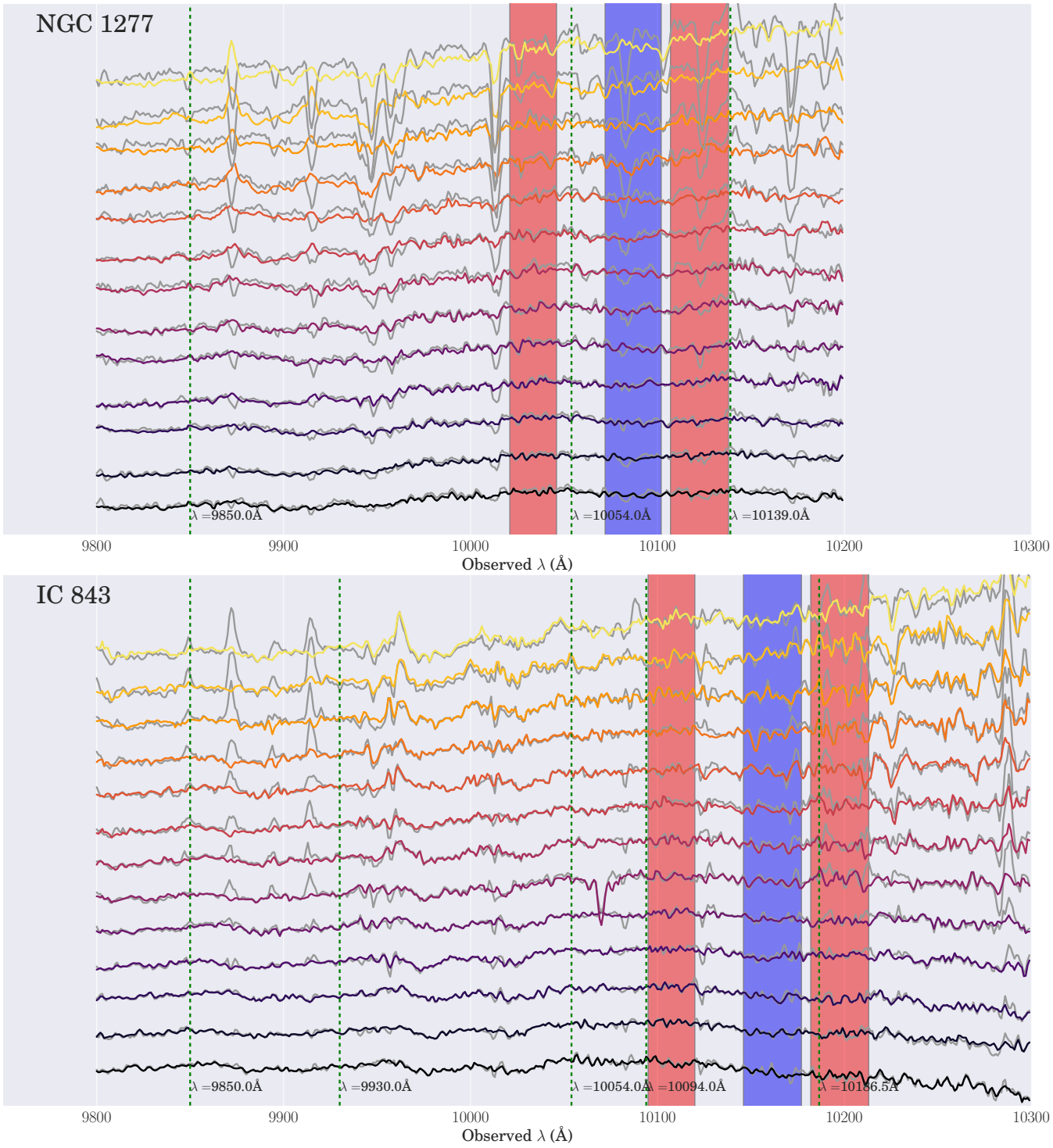

Figure A4. 13 spectra around the Wing-Ford band for both NGC 1277 (top) and IC 843 (bottom). These 13 spectra correspond to a central bin and 6 spectra each from the left and right sides of the galaxy. The 7 radial bins for each galaxy we use to measure index equivalent widths are formed by interpolating each of these spectra to their rest frame and adding them. The lines correspond to the spectrum in each bin before `pPXF` sky subtraction (but after first order sky subtraction; coloured grey) and afterwards (black through yellow). The spectra range from the central bin (bottom, dark) to the outermost (top, light). Green dashed line indicate the position of a cut to the sky spectrum. Blue shaded regions show the location of the FeH index whilst red shaded regions identify the location of the continuum regions.

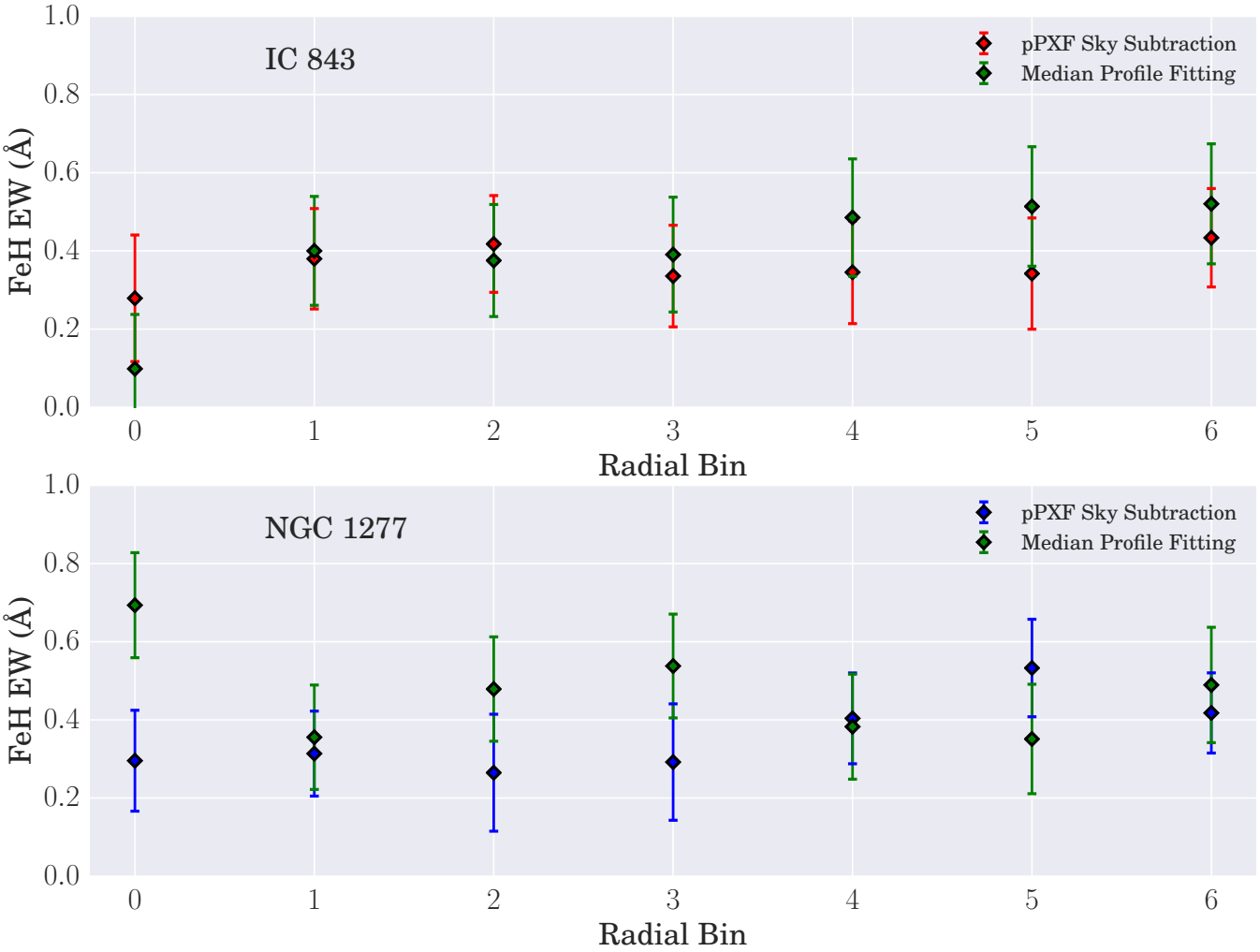

Figure A5. Comparison of equivalent width measurements of the Wing-Ford band after `pPXF` sky subtraction and median profile fitting. The two methods give good agreement, confirming the robustness of our results.

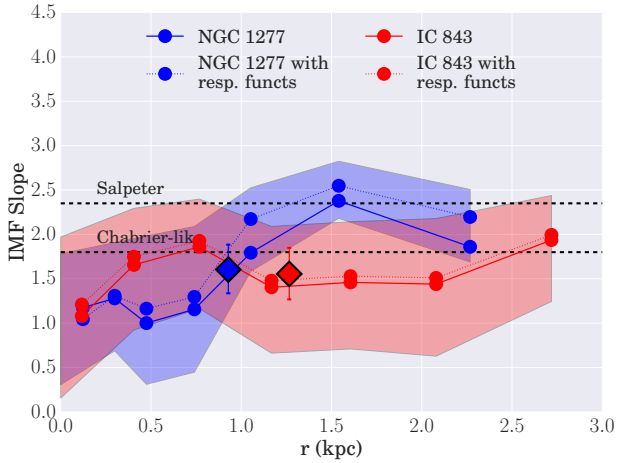

Figure B1. Same as Figure 9 except including response functions. IMF slope against radius for NGC 1277 (blue) and IC 843 (red). Diamonds correspond to IMF slope found using the global measurement in each galaxy. The solid line shows the IMF slope found at each radius without response functions whilst the dotted line includes them. Shaded regions are around the dotted line, and show 1-σ uncertainties. The measured FeH equivalent width leads to Chabrier-like unimodal IMFs at all radii in both galaxies, with only marginal evidence for an IMF gradient in the outskirts of NGC 1277. See section 6.2 for details.

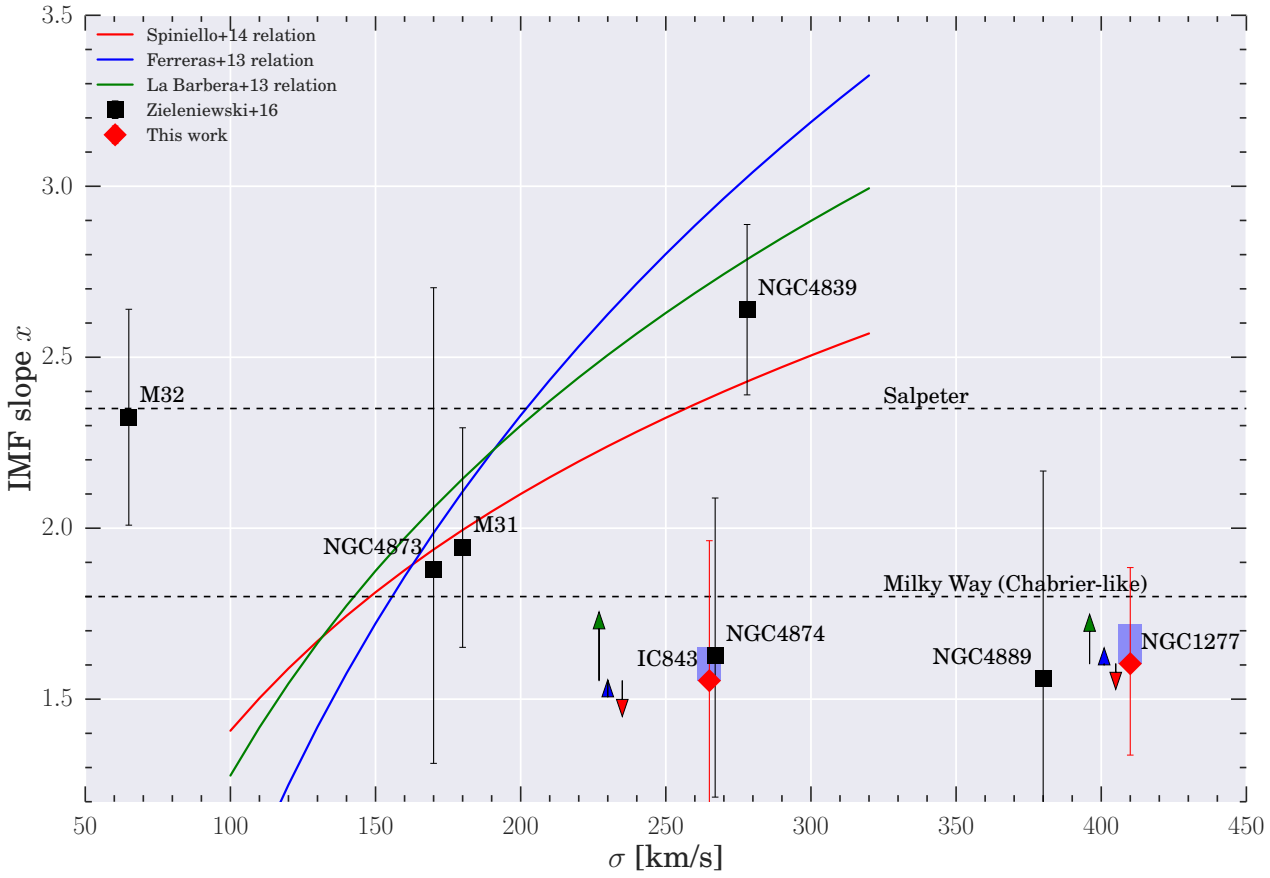

Figure B2. IMF slope against velocity dispersion for the galaxies studied in this work, Zieleniewski et al. (2015) and Zieleniewski et al. (2016). Coloured lines show proposed IMF-σ relationships from Spiniello et al. (2014), Ferreras et al. (2013) and La Barbera et al. (2013b) . Blue shaded regions show the overall effect of including response functions to model changes in [α/Fe] (green arrow), [Na/Fe] (blue arrow) and [Fe/H] (red arrow) on NGC 1277 and IC 843.